

Gelatin-Coated Copper-Based Metal–Organic Framework for Controlled Insulin Delivery: Possibility toward Oral Delivery System

Pawan Kumar, Navpreet Kaur, Pranav Tiwari, Anoop Kumar Gupta, and Shaikh M. Mobin*



Cite This: *ACS Materials Lett.* 2023, 5, 1100–1108



Read Online

ACCESS |



Metrics & More

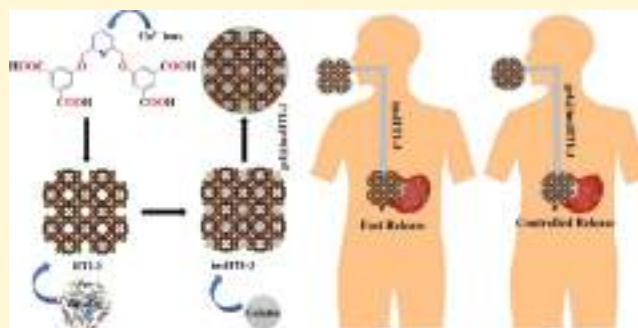


Article Recommendations



Supporting Information

ABSTRACT: The development of nontoxic, hemocompatible materials for controlled insulin delivery is a great challenging task for researchers. Herein, we demonstrate the design of a novel linker 5,5'-((pyridine-2,6-diylbis(methylene)) bis(oxy)-diisophthalic acid (H_4L) and its utilization to synthesize a new Cu-MOF (IITI-3). IITI-3 crystallizes in a tetragonal crystal system with space group $I4/mmm$ and shows a high Brunauer–Emmett–Teller (BET) surface area of $1026.5\text{ m}^2/\text{g}$ with pore diameter (Barrett–Joyner–Halenda pore size distribution) of 3.413 nm . The IITI-3 is found to be stable in the biological fluid pH ranges from 3 to 10. Moreover, IITI-3 were explored for insulin delivery by coating the IITI-3 with gelatin (gel@insIITI-3); the overall insulin was controlled from the framework. The obtained result paves a new avenue for the oral delivery of insulin using the IITI-3 metal-organic framework.



INTRODUCTION

Diabetes mellitus (DM) is the most challenging disease¹ and mainly occurs in two types: type I (T1DM) and type II (T2DM). In T1DM, the body does not produce enough insulin, and contrarily T1DM is also known as insulin resistance in which either the body fails to produce insulin or shows resistance toward insulin.² Beta cells are responsible for the production of insulin in the body. In T1DM, the autoimmune system kills the beta cells resulting in less or no production of insulin.³ Hyperglycemia occurs when there is an excess of glucose in the blood and the body does not produce or use enough insulin in the case of T2DM.⁴ T2DM significantly increases the risk of both macrovascular alterations and microvascular consequences, such as retinopathy, neuropathy, and nephropathy.^{5–8} Different medicines have been developed to treat T1DM and T2DM, but direct insulin injection continues to be the only therapeutic option that is currently effective for patients.⁹ Good glycemic control in T1DM typically necessitates at least two (and frequently three or more) daily insulin injections.^{10,11} Therefore, the development of oral insulin delivery systems is required to lessen the discomfort and pain experienced by patients who frequently consume insulin subcutaneously via injection. The subcutaneously injected insulin may cause peripheral hyperinsulinemia and related problems, but when administered orally is more capable of passing through the liver similarly to physiologically

produced insulin.¹² However, oral medication distribution has severe complications, including issues with stability in the gastrointestinal (GI) tract, solubility, bioavailability, and dissolution. Several oral insulin formulations have undergone clinical testing; however, substantial commercial development has not yet been accomplished.¹³

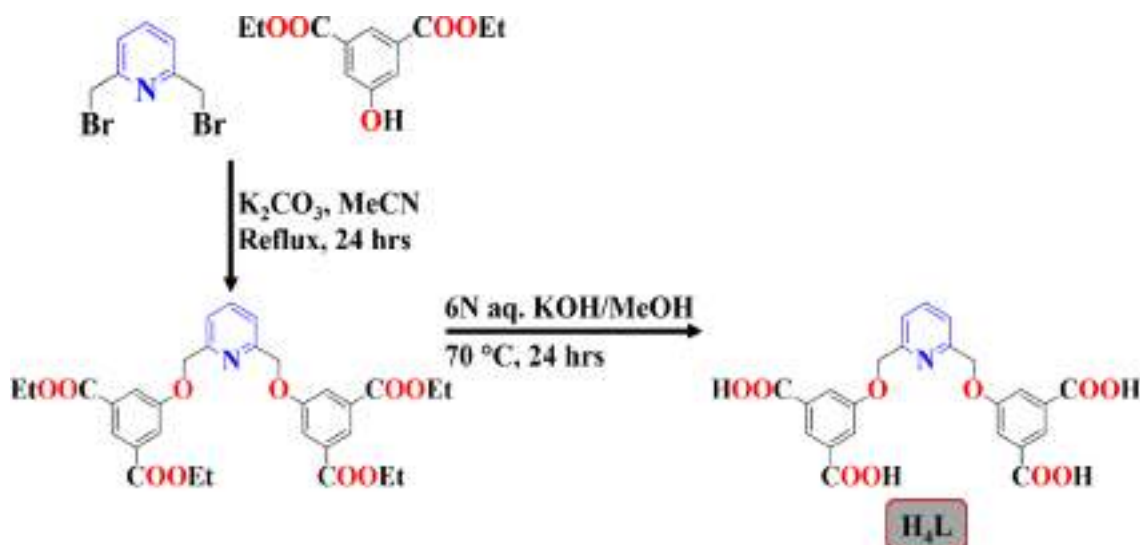
The proposed system must include a biocompatible, high-loading platform that protects insulin from external acidic environments and enzymatic degradation, as well as targeted drug delivery coupled with stimuli-responsive drug release, such as hyperglycemia, in order to be considered an efficient oral insulin delivery method.¹⁴ Currently, various materials are employed for oral delivery (such as liposomes, nanoemulsions, nanoparticles, or micelles)^{15–18} but they are largely ineffective; improved methods are therefore required to solve the drawbacks. Recently, the metal–organic-frameworks (MOFs) have established themselves as an exciting candidate for different biomedical applications such as drug delivery, bioimaging and sensing etc. because of their tunable size,

Received: December 13, 2022

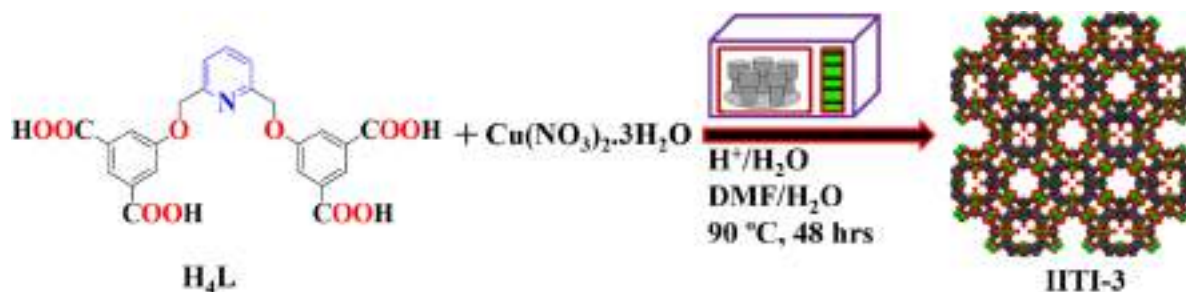
Accepted: March 8, 2023

Published: March 10, 2023



Scheme 1. Schematic Synthesis of H₄L

Scheme 2. Schematic Synthesis of IITI-3



high porosity, and range of starting materials.^{19–22} Among different biomedical applications of MOF, its suitability toward drug delivery can be more diverse and impactful because it can encapsulate different therapeutic molecules in their cavities with high loading and then can deliver drugs in a controlled manner; because of the release of the drug molecule from the framework, it takes more time, because of the breaking of interactions between framework and drug molecules, which usually cannot be possible with different other nano/biomaterials. MOFs themselves are well-known for controlled drug release, because drug are stored within the pores, on the surface of the framework, and upheld by the electrostatic interaction (hydrophilic or hydrophobic), hydrogen bonding, van der Waals, the π - π interaction, coordination bonds, and anion-cation electrostatic interaction.^{23,24} Generally, the Co-, Ni-, and Cr-based MOFs revealed in these studies were incompatible with biological and pharmacological applications, due to the toxic nature of metal present within the framework. However, in the case of ionic drugs, the strong electrostatic interaction between ionic drugs and ionic frameworks plays a crucial role.²⁵ Large surface area and high porosity (mesoporous and macroporous) of MOFs is necessary condition for high drug loading, large protein molecules encapsulation. Cu-MOFs, Fe-MOFs, and Zn-MOFs are highly biocompatible, hemocompatible, and biodegradable in nature. But most of the MOFs degrades in a wide range of pH (3–10), and also are not stable in the medium. Apart from that most of the framework is losing their identity after gelatin coating. Upon comparing MOFs with chitosan-based nanocomposites,

they have less surface area, are unstable at alkaline pH, and do not have tunable pore size; however, in the case of MOFs, they have high surface area and are stable over a wide range of pH, from acidic to alkaline.^{26,27} Additionally, MOFs can keep proteins active in hostile environments like stomach fluid (pH 1.5–3.5), simulated physiological conditions (pH 7.2–7.4), and organic solvents.^{28–30}

Currently, the sustainable release of drugs from MOFs have gained considerable interest.³¹ However, three primary approaches have been employed up to this point: (i) coating-controlled drug release; (ii) drug release regulated by drug-matrix interaction, and (iii) drug release initiated by cations.^{32,33} In the coating-controlled drug release method, majorly synthetic or natural polymeric materials are used to create microparticulate delivery systems. Gelatin is one of the natural polymers, which is used extensively in the pharmaceutical industry, because of its outstanding biocompatible nature, excellent degradability to nontoxic chemicals, and low cost.^{34,35} Gelatin also increases the biocompatibility of materials. In 2019, Nezhad-Mokhtari et al.³⁶ performed methotrexate delivery via gelatin-coated Cu-MOF in a very sustainable manner. Similarly, in 2019, Javanbakht et al.³⁷ performed ibuprofen oral delivery via gelatin-coated Cu-MOF in a controlled manner.

Herein, we have designed/synthesized a new three-dimensional (3D) Cu-MOF named IITI-3 utilized for drug encapsulation by insulin and Hum-insulin (insulin that is commercially available). After encapsulation with insulin, termed as *insIITI-3*, and further coated with gelatin formed

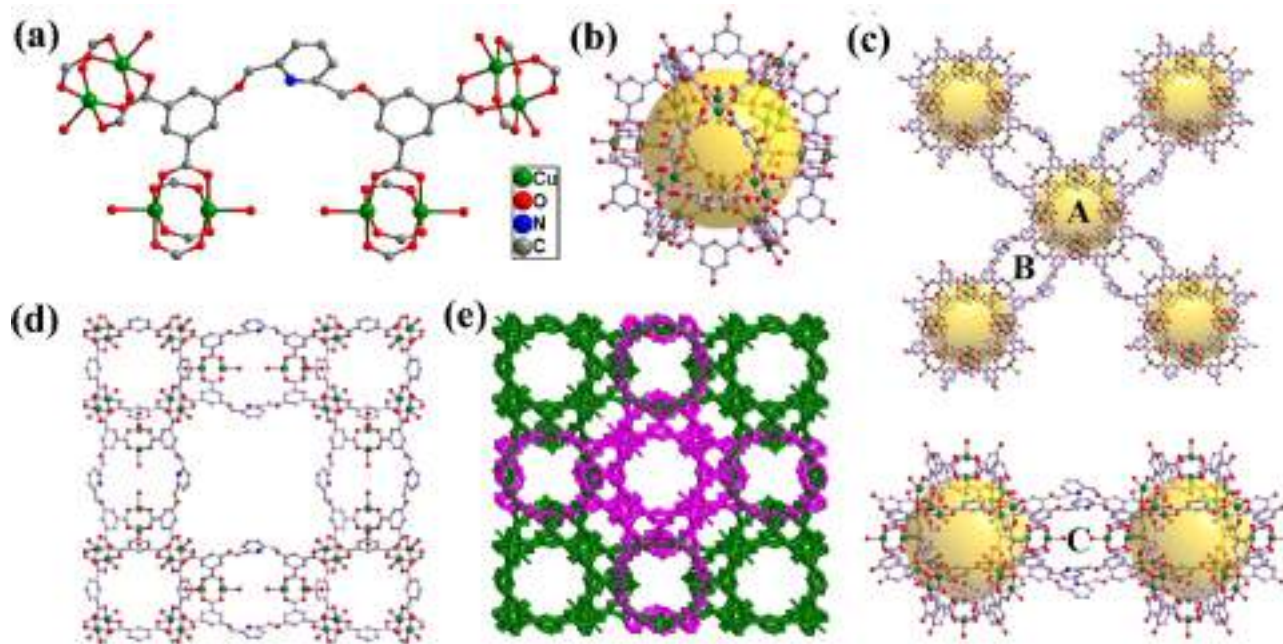


Figure 1. (a) H_4L ligand with Cu^{2+} ions to form IITI-3 containing $[Cu_2(COO)_4]$ SBUs, (b) interconnection of 12 such SBUs produces a typical metal–organic cuboctahedron (MOC, cavity A), (c) interconnection of MOCs in the *ab*-plane and *c*-axis by H_4L units. (d) Illustration of the 3D framework along the *c*-axis, and (e) 2-fold interpenetrated 3D frameworks.

as **gel@insIITI-3** to explore its release pattern in different pH conditions toward their control release.

A novel tetracarboxylic acid linker H_4L was synthesized by the substitution reaction of 2,6-(bisbromomethyl)pyridine, and 5-hydroxyisophthalate in the presence of K_2CO_3 in acetonitrile solvent, followed by basic hydrolysis resulting in the formation of H_4L , which is well-characterized by high-resolution mass spectrometry (HRMS) and nuclear magnetic resonance (NMR) spectroscopy [Scheme 1; the detailed synthetic procedure is given in the Supporting Information (SI) (Figures S1–S6)].

The solvothermal reaction of the novel tetracarboxylic acid linker (H_4L) and $Cu(NO_3)_2 \cdot 3H_2O$ in a mixed solvent system (DMF + H_2O) under a Teflon-lined autoclave resulted in a blue-colored block-shaped single crystals of **IITI-3** (Scheme 2; the detailed synthetic procedure is given in the SI).

The single-crystal X-ray diffraction (SCXRD) studies of **IITI-3** reveal that it crystallizes in the tetragonal $I4/mmm$ space group (Table S1 in the SI). In the framework of **IITI-3**, both isophthalate units of the H_4L linker utilizes four carboxylate groups to link eight Cu(II) ions which are further extended through the coordination of carboxylate groups from the other H_4L linkers. All the Cu(II) ions are equatorially coordinated by carboxylate's oxygens from the different H_4L linkers [Cu–O: 1.944(4)–1.962(6) Å] and axially occupied by water molecules [Cu–O: 2.094(10)–2.147(8) Å (Table S2 in the SI), leading to a square pyramidal geometry.

The combination of two such square pyramidal Cu(II) centers forms a typical inorganic paddlewheel (PW) $[Cu_2(COO)_4 \cdot 2H_2O]$ as secondary building units (SBUs) with the Cu–Cu separation of 2.6477(14)–2.6549(18) Å (Table S2) (Figure 1a). Again, such units are extended through Cu(II)–OOC linkage to generate a highly porous framework called metal–organic cuboctahedron (MOC) that contains three types of microporous cavities: A, B, and C (Figures 1b and 1c). A closer view of the framework shows that

the isophthalate moiety of H_4L connects to two Cu_2 PW-SBUs; again, 12 such PW-SBUs were spanned by 24 isophthalate units from different H_4L linkers to produce edge-directed corner-linked MOCs containing cavity A (15.86 Å) (Figure 1c). The MOC consists of eight and six triangular and square windows, respectively, which will allow guest molecules to enter the interior cavities. The vicinal MOCs are further interconnected through the H_4L spacer producing two more types of cavities B and C (7.84 Å). The linking of two PW-SBUs by four H_4L units produces cavity B, and the linking of two clusters of four SBUs by four H_4L units produces cavity C. Furthermore, each MOC was interconnected with six neighboring MOCs through 24 H_4L moieties, resulting in four and two cavities of types B and C, respectively, surrounding each MOC. Additionally, **IITI-3** exhibits 2-fold interpenetration and generates a fourth pseudo-cavity that is filled with a MOC from the second framework (Figures 1d and 1e). However, the channels formed via the open windows of the MOC nodes and the C cavities persist along the *c*-axis. The channels were filled by disordered lattices solvent molecules, which were treated by SQUEEZE refinement of PLATON to calculate the effective solvent-accessible void volume and found to be 48.7% (Å³) per unit cell. The highly porous nature and larger cavities of **IITI-3** offer appropriate corridors for insulin loading and acting as a suitable cargo for insulin delivery.

The single-crystal structural studies reveals that the **IITI-3** has the larger cavity, i.e., cavity A ~ 16 Å in size. The particle size of monomeric insulin is 13 Å,³⁸ and, at pH 7.4, insulin forms tetramers 25 ± 3 Å in size.³⁹ Therefore, it could be possible that the monomeric insulin can fit in cavity A, and allowed insulin to diffuse through the framework and to be released from the MOF's cavities/pores.

Furthermore, we have used gelatin as coating material, because of its extensive use in the food, beauty, pharmaceutical industries, easy availability, and excellent structural stabil-

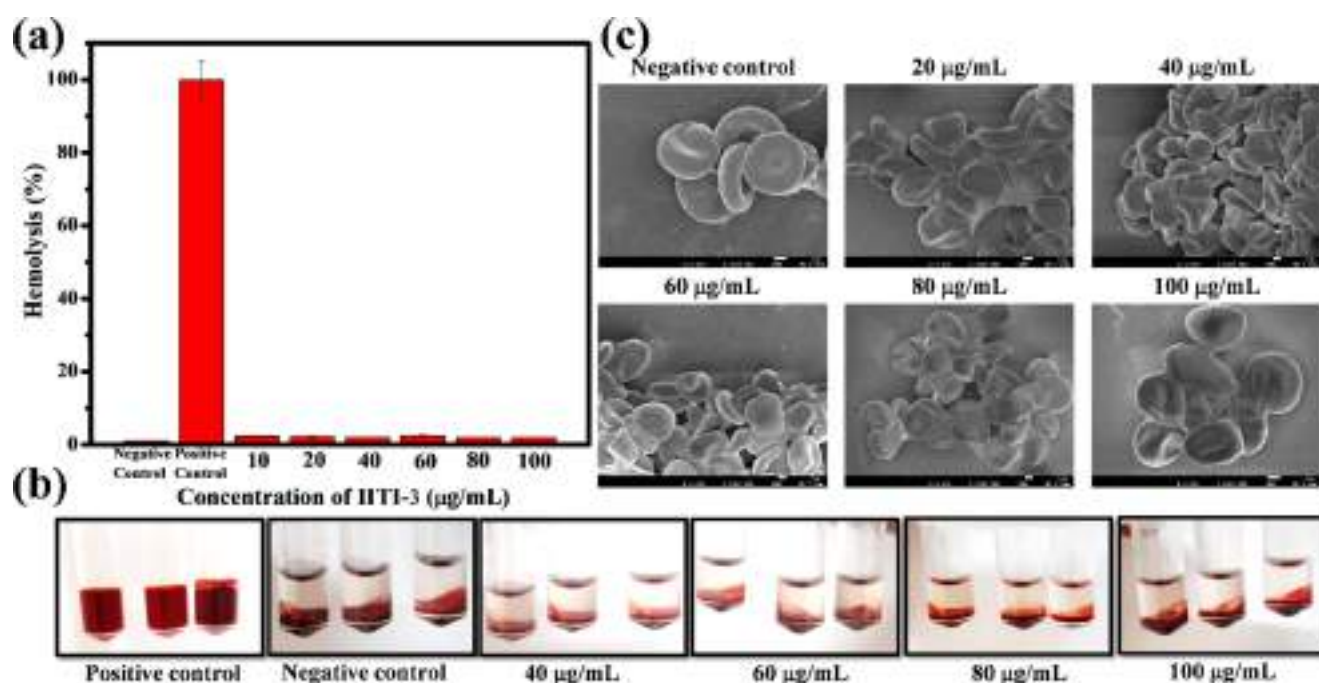


Figure 2. Hemocompatibility of IITI-3. (a) The percentage hemolysis graph after incubating RBCs with different concentrations of IITI-3 for 1 h, (b) the images of the centrifuged samples (control and treated), and (c) the SEM images of negative control and IITI-3-treated RBCs.

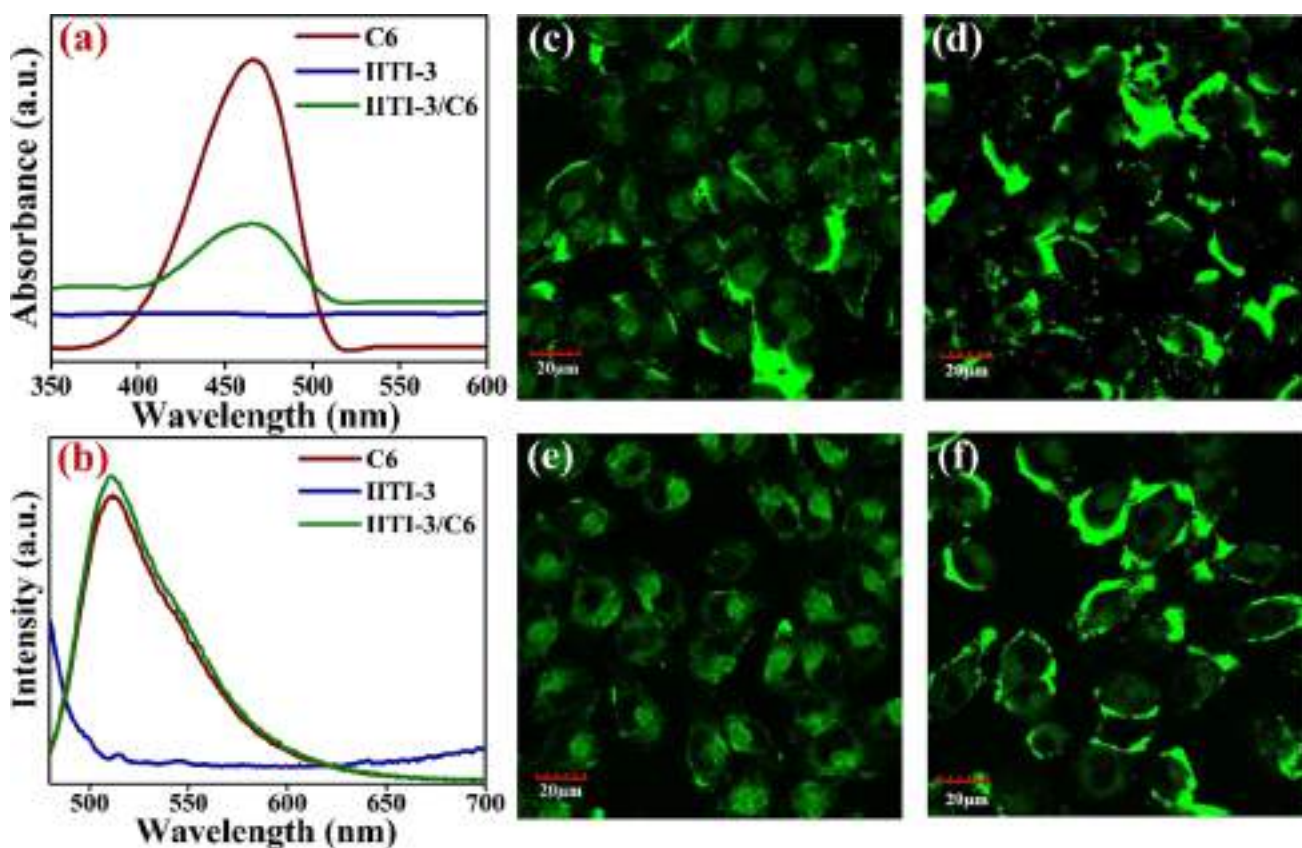


Figure 3. (a) UV-vis spectra of C6, IITI-3, and IITI-3/C6; (b) emission spectra of C6, IITI-3, and IITI-3/C6. In vitro cellular uptake assay: fluorescence ($\lambda_{\text{ex}}/\lambda_{\text{em}} = 488/520 \pm 25$ nm) images of cells treated with (c) IITI-3/C6, (d) insIITI-3/C6, (e) gel@IITI-3/C6, and (f) gel@insIITI-3/C6.

ity.^{40,41} Prior of applying IITI-3 for insulin delivery, its cellular and hemocompatibility studies were performed and detailed

explanation were provided in the SI (see Figures S7 and S8a). The effect of IITI-3 on the red blood cells (RBCs) was

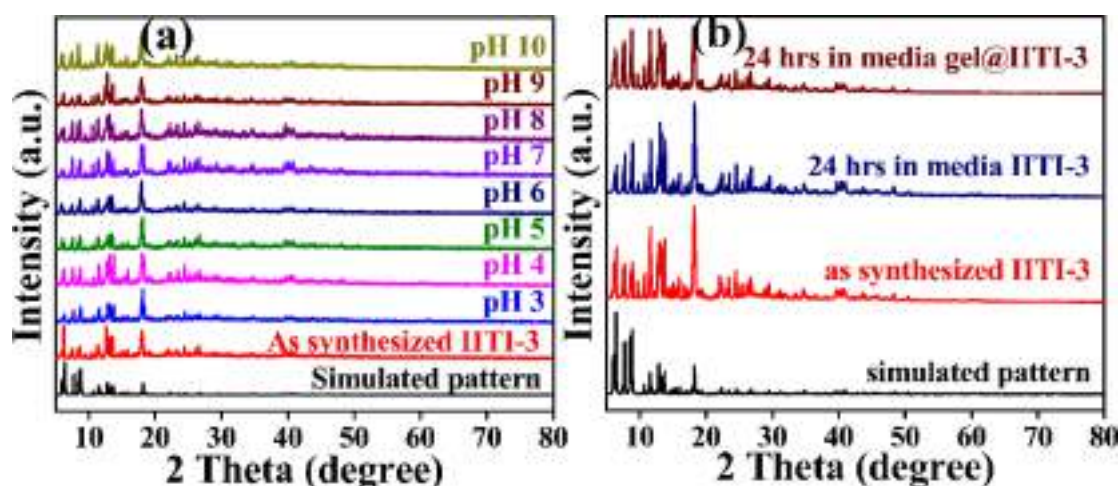


Figure 4. PXRD of IITI-3 (a) simulated, as synthesized, at different pH values from pH 3 to pH 10, and (b) simulated, as-synthesized, IITI-3 and gel@IITI-3 in media after treatment for 24 h.

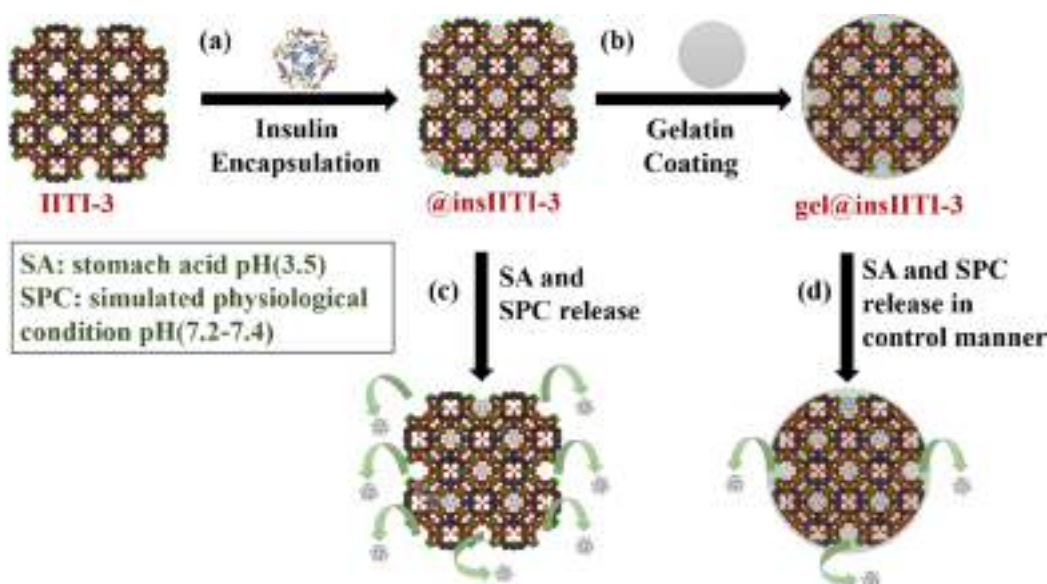


Figure 5. (a) Insulin encapsulation IITI-3 and the (b) gelatin coating on insIITI-3; panels (c) and (d) show insulin release profiles from insIITI-3 and gel@insIITI-3 in stomach acid and SPC pH, respectively.

checked through hemolysis assay. The result shown in Figure 2a clearly indicate the hemocompatible nature of IITI-3. Even the high concentration of IITI-3 showed very less hemolysis, i.e., <3%. The positive control clearly shows the red color of the supernatant generated by the presence of free hemoglobin, but the treated samples with IITI-3 lack any red supernatant color and resemble the color of the negative control (Figure 2b). Hemocompatible materials are those that exhibit <5% hemolysis. The biconcave shape of RBCs is further confirmed by the SEM images of RBCs treated with different concentrations of IITI-3, which further support the hemocompatible nature of IITI-3 and surface passivation therefore supports its nonhemolytic character (Figure 2c).⁴² The internalization of IITI-3, gel@IITI-3, insIITI-3, and gel@insIITI-3 in MCF-7 cells was checked for its effective cellular uptake by conjugating the framework with fluorescent dye C6 (Coumarin 6). As shown in Figure 3, the clear green fluorescence (bright-field images given in Figure S8b in the SI) arising from the cytoplasm of the treated cells shows the effective uptake of IITI-3, gel@IITI-3, insIITI-3, and gel@

insIITI-3. The C6 dye IITI-3 conjugation was confirmed using ultraviolet–visible light (UV-vis) spectroscopy and fluorescence spectroscopy. The new UV peak at ~470 nm of IITI-3/C6 coincide with the peak of C6. Similarly, in fluorescence spectroscopy, IITI-3/C6 exhibits a peak at 510 nm, which was coincide with C6 dye.

Apart from that, the structural stability of IITI-3 was also checked by powder X-ray diffraction (PXRD) (Figure 4a) and SEM images (Figure S9 in the SI) under different pH conditions (pH 3–10) to mimic simulated gastric fluid condition pH (pH 1.5–3.5) and simulated physiological condition (SPC) pH (7.2–7.4). The obtained result supported the “stability of IITI-3 at various physiological conditions” and motivated us to use them for insulin delivery. Furthermore, the stability of IITI-3 and gelatin coated gel@IITI-3 were checked in Dulbecco’s Modified Eagle Medium (DMEM) containing 10% fetal bovine serum (FBS). The IITI-3 and gelatin coated gel@IITI-3 were stable, even in the cell culture media, as shown in PXRD (Figure 4b).

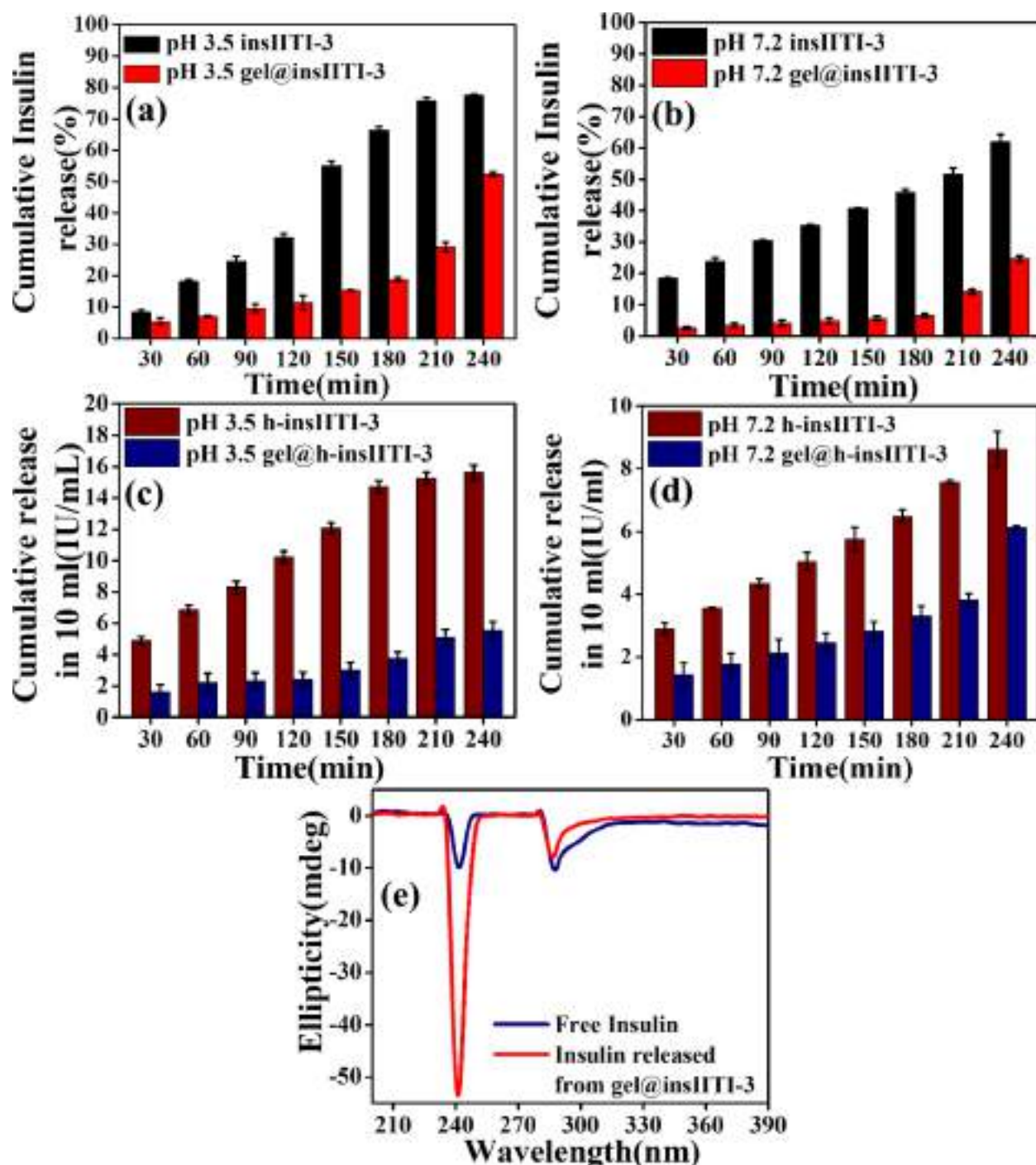


Figure 6. Cumulative insulin release from (a) insIITI-3 and gel@insIITI-3 at pH 3.5, (b) insIITI-3 and gel@insIITI-3 at pH 7.2, (c) h-insIITI-3 and gel@h-insIITI-3 at pH 3.5, (d) h-insIITI-3 and gel@h-insIITI-3 at pH 7, and (e) CD spectra of free insulin and insulin released from gel@insIITI-3.

IITI-3 showed all the effective attributes needed for an oral delivery nanocarrier. Because of good biocompatibility (stable in wide pH range (pH 3–10) and cell media) favors IITI-3 as a potential candidate as a drug delivery carrier with insulin. Also, by modifying the nanocarrier with high surface area ($1056.5 \text{ m}^2/\text{g}$), pore diameter (3.413 nm), (see Figures S10, S14d, and S14e in the SI), hemocompatibility with proteins/biomolecules offers advantages like “modulation of the immune response, variation of in vivo biodistribution and generation of stealth property”, which ultimately may improve

the delivery pattern.⁴³ Recently, Tian and co-workers⁴⁴ reported decorating UiO-68-NH₂ with transferrin for controlled insulin delivery. For the drug delivery phenomenon, the IITI-3 was encapsulated with insulin and for control release, it was further modified with gelatin. The schematic representation for the formation of ins@IITI-3 and gel@insIITI-3 is shown in Figures 5a and 5b. The IITI-3 was activated, further modified as insIITI-3 and gel@insIITI-3, which were characterized by PXRD, TGA, FT-IR, BET adsorption isotherm, and SEM (EDX). Their analysis is thoroughly

explained in the SI (see Figures S10–S17). The drug loading content (DLC) after insulin encapsulation (**insIITI-3**) was determined to be 20 wt% and also found to be in commercially available insulin (Hum-insulin). The DLC is calculated by measuring the absorbance of supernatant after loading via UV-vis spectroscopy and with the help of a linearity plot (see Figures S12 and S13 in the SI) by employing the DLC formula (eq S1 in the SI). Furthermore, DLS showed an increase in hydrodynamic diameter after gelatin coating in **IITI-3** (**gel@IITI-3**), which confirmed that gelatin is successfully covered throughout the surface of **IITI-3** (see Figure S18 in the Supporting Information). The zeta potential values of **IITI-3** and **gel@insIITI-3** are -20.8 mV and -12.40 mV, respectively (see Figure S19 in the Supporting Information).

Drug loading was confirmed by the increase in the weight percentage in TGA. From BET surface area and BJH pore size distribution, it has been confirmed that the pore size decreases from 3.412 nm to 3.406 nm and the surface area decreases from 1026.516 m²/g to 576.11 m²/g. It has been confirmed that the pore of the **IITI-3** that is filled with insulin decreases in surface area, which suggests that insulin is also present on the surface of the **IITI-3**. The possible reason for the insulin loading within the framework is either hydrophobic and/or electrostatic interaction between **IITI-3** and insulin molecules.³¹ Furthermore, gelatin coating has been performed on the **insIITI-3**. A drug release profile has been obtained via a dialysis method. The fast drug release from the **insIITI-3** has been related to the diffusion method.^{24,45,46} In this method, insulin comes out from the channel present inside to the **insIITI-3** to the solution. In stomach acid (pH 3.5), drug release is faster in comparison to SPC (pH 7.2); a possible reason is that the solubility of insulin increases as the pH decreases. However, in the case of gelatin-coated **insIITI-3** (**gel@insIITI-3**), drug release is regulated with the gelatin corona which covered the surface of the **insIITI-3**. Therefore, in this work, gelatin provide the barrier for insulin, which is releasing from **insIITI-3**. To examine the release profile of regular insulin (r-insulin) from **insIITI-3** and **gel@insIITI-3**, we have taken the solution of pH 3.5, and pH 7.2 (Figures 5c and 5d). These pH value corresponds to stomach acid (pH 1.5–3.5) and SPC (pH 7.2–7.4). The graphs shown in Figures 6a–d) indicate that both the **insIITI-3** and the **gel@insIITI-3** loaded with insulin have sustained-release characteristics. The developed carriers **insIITI-3** and **gel@insIITI-3** release insulin gradually and over a period of time, up to 4 h.

By comparison with Figures 6a–d, it is evident that the drug release from **IITI-3** could be regulated by using a polymer coating comprised of gelatin material. As the pH value increases, the percentage drug release decreases; this might be connected to the gelatin polymer's pH sensitivity and the gelatin microsphere polymeric network's diffusion barrier. The same pattern was observed in the case of Hum-insulin **h-insIITI-3** and **gel@h-insIITI-3** (Figures 6c and 6d). The gelatin-coated **IITI-3** gives controlled results with respect to time and rate, as compared to the recent reports (see Table S3 in the SI).

Using circular dichroism (CD) spectroscopy, the insulin conformational changes were assessed. As seen in Figure 6e, neither the insulin that was released from **gel@insIITI-3** nor the normal insulin underwent any substantial structural changes, demonstrating that the insulin maintenance was confirmed, even after its release.

CONCLUSION

In conclusion, in the present work, a new **Cu-MOF**, termed as **IITI-3**, were prepared solvo-thermally by utilizing a novel **H₄L** linker. Moreover, the **IITI-3** showed excellent structural stability, biocompatibility, and hemocompatibility. Also, because of its very high porosity, **IITI-3** had good protein-drug loading (insulin) (up to 20 wt %). Furthermore, coating the **insIITI-3** with gelatin gives more controlled release of insulin, compared to uncoating under physiological conditions. The gelatin coating on **insIITI-3** was done in a facile manner to amend the release pattern of encapsulated insulin, thus providing the synthesis advantages along with gelatin's own advantages. The insulin delivery from the framework after gelatin coating was ~50%, which was ~80% without coating at pH 3.5 and similar behavior at pH 7.2, suggesting that gelatin acts as an extra barrier for the insulin to get released. Thus, based on the release performance, good biocompatibility, hemocompatibility, and the presence of gelatin coating, we believe that **gel@insIITI-3** may be a potential candidate for an exciting possibility in the areas of protein and nucleic-acid-based oral delivery and can be extended for other diseases in the future.

ASSOCIATED CONTENT

Supporting Information

The Supporting Information is available free of charge at <https://pubs.acs.org/doi/10.1021/acsmaterialslett.2c01175>.

Experimental section including synthesis of **H₄L** linker and their characterizations (mass spectrometry, NMR spectroscopy), **IITI-3** (SC-XRD, PXRD, SEM, TGA, FT-IR, BET adsorption isotherm), cytotoxicity assay, and bright-field images; the activation of **IITI-3**, insulin encapsulation (**insIITI-3**), and modification with gelatin (**gel@insIITI-3**), which are characterized by PXRD, SEM (EDX), TGA, FT-IR, BET adsorption isotherm, DLS, and zeta potential; comparison table (PDF)

AUTHOR INFORMATION

Corresponding Author

Shaikh M. Mobin – Department of Chemistry, Indian Institute of Technology, Indore 453552, India; Department of Biosciences and Bio-Medical Engineering and Center for Electric Vehicle and Intelligent Transport Systems, Indian Institute of Technology Indore, Indore 453552, India; orcid.org/0000-0003-1940-3822; Phone: +91-731-2438752; Email: xray@iiti.ac.in

Authors

Pawan Kumar – Department of Chemistry, Indian Institute of Technology, Indore 453552, India

Navpreet Kaur – Department of Biosciences and Bio-Medical Engineering, Indian Institute of Technology Indore, Indore 453552, India

Pranav Tiwari – Department of Chemistry, Indian Institute of Technology, Indore 453552, India

Anoop Kumar Gupta – Department of Chemistry, Indian Institute of Technology, Indore 453552, India; Department of Chemistry, Pandit Prithi Nath College (C. S. J. M. University), Kanpur 208001 Uttar Pradesh, India

Complete contact information is available at:

<https://pubs.acs.org/doi/10.1021/acsmaterialslett.2c01175>

Notes

The authors declare no competing financial interest.

ACKNOWLEDGMENTS

P.K. would like to thank Ministry of Education, Government of India for providing research fellowship. N.K. thanks UGC New Delhi for a fellowship. P.T. thanks BRNS (Project No. 58/14/17/2020-BRNS/37215). A.K.G. thanks IIT Indore for an Institute Postdoc fellowship. Additionally, A.K.G. sincerely acknowledges P. P. N. College Kanpur for research facilities and infrastructure. S.M.M. acknowledge SERB (CRG/2020/001769), BRNS (Project No. 58/14/17/2020-BRNS/37215) and IIT Indore for financial support. The authors gratefully acknowledge Dr. Ravinder, Mr. Kinny Pandey, Mr. Ghan-shyam Bhavsar, and Mr. Nitin Upadhyay (Sophisticated Instrumentation Centre, IIT Indore) for characterization facilities. Authors are also thankful to Material Research Centre, MNIT Jaipur for providing the zeta potential facility. P.K. also thanks Dr. Viresh Kumar and Praveen Kumar for their help during manuscript preparation.

ABBREVIATIONS

DMF, dimethylformamide; MeOH, methanol; KOH, potassium hydroxide; CD, circular dichroism; DLS, dynamic light scattering; SI, Supporting Information

REFERENCES

- (1) Moawd, S. A. Quality of Life in University Students with Diabetes Distress: Type 1 and Type 2 of Diabetes Differences. *J. Diabetes Res.* **2022**, 2022, 1–7.
- (2) Jiang, H.; Pang, S.; Zhang, Y.; Yu, T.; Liu, M.; Deng, H.; Li, L.; Feng, L.; Song, B.; Han-Zhang, H.; Ma, Q.; Qian, L.; Yang, W. A Phase 1b Randomised Controlled Trial of a Glucagon-like Peptide-1 and Glucagon Receptor Dual Agonist IB1362 (LY3305677) in Chinese Patients with Type 2 Diabetes. *Nat. Commun.* **2022**, 13, 3613.
- (3) Liu, R.; Liu, C.; He, X.; Sun, P.; Zhang, B.; Yang, H.; Shi, W.; Ruan, Q. MicroRNA-21 Promotes Pancreatic β Cell Function through Modulating Glucose Uptake. *Nat. Commun.* **2022**, 13, 3545.
- (4) Ukah, U. V.; Platt, R. W.; Auger, N.; Dasgupta, K.; Dayan, N. Development and Internal Validation of a Model to Predict Type 2 Diabetic Complications after Gestational Diabetes. *Sci. Rep.* **2022**, 12, 10377.
- (5) Rad, M. G.; Sharifi, M.; Meamar, R.; Soltani, N. The Role of Pancreas to Improve Hyperglycemia in STZ-Induced Diabetic Rats by Thiamine Disulfide. *Nutr. Diabetes* **2022**, 12, 32.
- (6) Volpatti, L. R.; Matranga, M. A.; Cortinas, A. B.; Delcassian, D.; Daniel, K. B.; Langer, R.; Anderson, D. G. Glucose-Responsive Nanoparticles for Rapid and Extended Self-Regulated Insulin Delivery. *ACS Nano* **2020**, 14, 488–497.
- (7) Zhao, Y.; Trewyn, B. G.; Slowing, I. I.; Lin, V. S.-Y. Mesoporous Silica Nanoparticle-Based Double Drug Delivery System for Glucose-Responsive Controlled Release of Insulin and Cyclic AMP. *J. Am. Chem. Soc.* **2009**, 131, 8398–8400.
- (8) Au, K. M.; Tisch, R.; Wang, A. Z. *In Vivo* Bioengineering of Beta Cells with Immune Checkpoint Ligand as a Treatment for Early-Onset Type 1 Diabetes Mellitus. *ACS Nano* **2021**, 15, 19990–20002.
- (9) Cho, N. H.; Shaw, J. E.; Karuranga, S.; Huang, Y.; da Rocha Fernandes, J. D.; Ohlrogge, A. W.; Malanda, B. IDF Diabetes Atlas: Global Estimates of Diabetes Prevalence for 2017 and Projections for 2045. *Diabetes Res. Clin. Pract.* **2018**, 138, 271–281.
- (10) Khan, M. A. B.; Hashim, M. J.; King, J. K.; Govender, R. D.; Mustafa, H.; al Kaabi, J. Epidemiology of Type 2 Diabetes – Global Burden of Disease and Forecasted Trends. *J. Epidemiol. Glob. Health* **2020**, 10, 107.
- (11) Kikkawa, R. Chronic Complications in Diabetes Mellitus. *Br. J. Nutr.* **2000**, 84, 183–185.
- (12) Porte, D., Jr. Clinical Importance of Insulin Secretion and Its Interaction with Insulin Resistance in the Treatment of Type 2 Diabetes Mellitus and Its Complications. *Diabetes Metab. Res. Rev.* **2001**, 17, 181–188.
- (13) Al-Tabakha, M.; Arida, A. Recent Challenges in Insulin Delivery Systems: A Review. *Indian J. Pharm. Sci.* **2008**, 70, 278.
- (14) Skyler, J. S.; Cefalu, W. T.; Kourides, I. A.; Landschulz, W. H.; Balagtas, C. C.; Cheng, S.-L.; Gelfand, R. A. Efficacy of Inhaled Human Insulin in Type 1 Diabetes Mellitus: A Randomised Proof-of-Concept Study. *Lancet* **2001**, 357, 331–335.
- (15) Benyettou, F.; Kaddour, N.; Prakasam, T.; Das, G.; Sharma, S. K.; Thomas, S. A.; Bekhti-Sari, F.; Whelan, J.; Alkhalifah, M. A.; Khair, M.; Traboulsi, H.; Pasricha, R.; Jagannathan, R.; Mokhtari-Soulimane, N.; Gándara, F.; Trabolsi, A. *In Vivo* Oral Insulin Delivery via Covalent Organic Frameworks. *Chem. Sci.* **2021**, 12, 6037–6047.
- (16) Chaturvedi, K.; Ganguly, K.; Nadagouda, M. N.; Aminabhavi, T. M. Polymeric Hydrogels for Oral Insulin Delivery. *J. Controlled Release* **2013**, 165, 129–138.
- (17) Chen, M.-C.; Sonaje, K.; Chen, K.-J.; Sung, H.-W. A Review of the Prospects for Polymeric Nanoparticle Platforms in Oral Insulin Delivery. *Biomaterials* **2011**, 32, 9826–9838.
- (18) Bai, Y.; Zhang, Z.; Zhang, A.; Chen, L.; He, C.; Zhuang, X.; Chen, X. Novel Thermo- and PH-Responsive Hydroxypropyl Cellulose- and Poly (l-Glutamic Acid)-Based Microgels for Oral Insulin Controlled Release. *Carbohydr. Polym.* **2012**, 89, 1207–1214.
- (19) Lopes, M.; Abraham, B.; Seica, R.; Veiga, F.; Rodrigues, C.; Ribeiro, A. Intestinal Uptake of Insulin Nanoparticles: Facts or Myths? *Curr. Pharm. Biotechnol.* **2014**, 15, 629–638.
- (20) Huang, L.-L.; Yu, L.; Li, B.; Li, B.; Wang, H.; Li, J. Adsorption and Release of 1-Methylcyclopropene by Metal–Organic Frameworks for Fruit Preservation. *ACS Mater. Lett.* **2022**, 4, 1053–1057.
- (21) Zhou, Y.; Liu, L.; Cao, Y.; Yu, S.; He, C.; Chen, X. A Nanocomposite Vehicle Based on Metal–Organic Framework Nanoparticle Incorporated Biodegradable Microspheres for Enhanced Oral Insulin Delivery. *ACS Appl. Mater. Interfaces* **2020**, 12, 22581–22592.
- (22) Gupta, A. K.; Tomar, K.; Bharadwaj, P. K. Cd(ii) Coordination Polymers Constructed with a Flexible Carboxylate Linker and Pyridyl Co-Linkers: Variation in the Network Topologies and Photoluminescence Properties. *CrystEngComm* **2017**, 19, 2253–2263.
- (23) Horcajada, P.; Chalati, T.; Serre, C.; Gillet, B.; Sebrie, C.; Baati, T.; Eubank, J. F.; Heurtaux, D.; Clayette, P.; Kreuz, C.; Chang, J.-S.; Hwang, Y. K.; Marsaud, V.; Bories, P.-N.; Cynober, L.; Gil, S.; Férey, G.; Couvreur, P.; Gref, R. Porous Metal–Organic-Framework Nanoscale Carriers as a Potential Platform for Drug Delivery and Imaging. *Nat. Mater.* **2010**, 9, 172–178.
- (24) Rojas, S.; Colinet, L.; Cunha, D.; Hidalgo, T.; Salles, F.; Serre, C.; Guillou, N.; Horcajada, P. Toward Understanding Drug Incorporation and Delivery from Biocompatible Metal–Organic Frameworks in View of Cutaneous Administration. *ACS Omega* **2018**, 3, 2994–3003.
- (25) Férey, G. Hybrid Porous Solids: Past, Present, Future. *Chem. Soc. Rev.* **2008**, 37, 191–214.
- (26) Luo, W.; Bai, Z.; Zhu, Y. Fast Removal of Co(ii) from Aqueous Solution Using Porous Carboxymethyl Chitosan Beads and Its Adsorption Mechanism. *RSC Adv.* **2018**, 8, 13370–13387.
- (27) Prabakaran, M.; Mano, J. F. Chitosan-Based Particles as Controlled Drug Delivery Systems. *Drug Delivery* **2004**, 12, 41–57.
- (28) Peer, D.; Karp, J. M.; Hong, S.; Farokhzad, O. C.; Margalit, R.; Langer, R. Nanocarriers as an Emerging Platform for Cancer Therapy. *Nat. Nanotechnol.* **2007**, 2, 751–760.
- (29) Couvreur, P.; Gref, R.; Andrieux, K.; Malvy, C. Nanotechnologies for Drug Delivery: Application to Cancer and Auto-immune Diseases. *Prog. Solid State Chem.* **2006**, 34, 231–235.
- (30) Gref, R.; Minamitake, Y.; Peracchia, M. T.; Trubetskoy, V.; Torchilin, V.; Langer, R. Biodegradable Long-Circulating Polymeric Nanospheres. *Science* (1979) **1994**, 263 (263), 1600–1603.

- (31) Chen, Y.; Li, P.; Modica, J. A.; Drout, R. J.; Farha, O. K. Acid-Resistant Mesoporous Metal–Organic Framework toward Oral Insulin Delivery: Protein Encapsulation, Protection, and Release. *J. Am. Chem. Soc.* **2018**, *140*, 5678–5681.
- (32) Duan, Y.; Ye, F.; Huang, Y.; Qin, Y.; He, C.; Zhao, S. One-Pot Synthesis of a Metal–Organic Framework-Based Drug Carrier for Intelligent Glucose-Responsive Insulin Delivery. *Chem. Commun.* **2018**, *54*, 5377–5380.
- (33) Suresh, K.; Matzger, A. J. Enhanced Drug Delivery by Dissolution of Amorphous Drug Encapsulated in a Water Unstable Metal–Organic Framework (MOF). *Angew. Chem., Int. Ed.* **2019**, *58*, 16790–16794.
- (34) Wu, M.-X.; Yang, Y.-W. Metal–Organic Framework (MOF)-Based Drug/Cargo Delivery and Cancer Therapy. *Adv. Mater.* **2017**, *29*, 1606134.
- (35) della Rocca, J.; Liu, D.; Lin, W. Nanoscale Metal–Organic Frameworks for Biomedical Imaging and Drug Delivery. *Acc. Chem. Res.* **2011**, *44*, 957–968.
- (36) Nezhad-Mokhtari, P.; Arsalani, N.; Javanbakht, S.; Shaabani, A. Development of Gelatin Microsphere Encapsulated Cu-Based Metal–Organic Framework Nanohybrid for the Methotrexate Delivery. *J. Drug Delivery Sci. Technol.* **2019**, *50*, 174–180.
- (37) Javanbakht, S.; Nezhad-Mokhtari, P.; Shaabani, A.; Arsalani, N.; Ghorbani, M. Incorporating Cu-Based Metal–Organic Framework/Drug Nanohybrids into Gelatin Microsphere for Ibuprofen Oral Delivery. *Mater. Sci. Eng.: C* **2019**, *96*, 302–309.
- (38) Horcajada, P.; Serre, C.; Vallet-Regí, M.; Sebba, M.; Taulelle, F.; Férey, G. Metal–Organic Frameworks as Efficient Materials for Drug Delivery. *Angew. Chem., Int. Ed.* **2006**, *45*, 5974–5978.
- (39) Nielsen, L.; Frokjaer, S.; Brange, J.; Uversky, V. N.; Fink, A. L. Probing the Mechanism of Insulin Fibril Formation with Insulin Mutants. *Biochemistry* **2001**, *40*, 8397–8409.
- (40) Liu, K.; Zhang, J.-J.; Cheng, F.-F.; Zheng, T.-T.; Wang, C.; Zhu, J.-J. Green and Facile Synthesis of Highly Biocompatible Graphene Nanosheets and Its Application for Cellular Imaging and Drug Delivery. *J. Mater. Chem.* **2011**, *21*, 12034.
- (41) Tiwari, P.; Kaur, N.; Sharma, V.; Mobin, S. M. High-Yield Graphene Produced from the Synergistic Effect of Inflated Temperature and Gelatin Offers High Stability and Cellular Compatibility. *Phys. Chem. Chem. Phys.* **2018**, *20*, 20096–20107.
- (42) Kaur, N.; Sharma, V.; Tiwari, P.; Saini, A. K.; Mobin, S. M. Vigna Radiata” Based Green C-Dots: Photo-Triggered Theranostics, Fluorescent Sensor for Extracellular and Intracellular Iron(III) and Multicolor Live Cell Imaging Probe. *Sens. Actuators B Chem.* **2019**, *291*, 275–286.
- (43) Bellido, E.; Hidalgo, T.; Lozano, M. V.; Guillevis, M.; Simón-Vázquez, R.; Santander-Ortega, M. J.; González-Fernández, A.; Serre, C.; Alonso, M. J.; Horcajada, P. Heparin-Engineered Mesoporous Iron Metal–Organic Framework Nanoparticles: Toward Stealth Drug Nanocarriers. *Adv. Healthc. Mater.* **2015**, *4*, 1246–1257.
- (44) Zou, J.-J.; Wei, G.; Xiong, C.; Yu, Y.; Li, S.; Hu, L.; Ma, S.; Tian, J. Efficient Oral Insulin Delivery Enabled by Transferrin-Coated Acid-Resistant Metal–Organic Framework Nanoparticles. *Sci. Adv.* **2022**, *8* (8), abm4677.
- (45) Souza, B. E.; Donà, L.; Titov, K.; Bruzzese, P.; Zeng, Z.; Zhang, Y.; Babal, A. S.; Möslin, A. F.; Frogley, M. D.; Wolna, M.; Cinque, G.; Civalieri, B.; Tan, J.-C. Elucidating the Drug Release from Metal–Organic Framework Nanocomposites via In Situ Synchrotron Microspectroscopy and Theoretical Modeling. *ACS Appl. Mater. Interfaces* **2020**, *12*, 5147–5156.
- (46) Li, Z.; Peng, Y.; Xia, X.; Cao, Z.; Deng, Y.; Tang, B. Sr/PTA Metal Organic Framework as A Drug Delivery System for Osteoarthritis Treatment. *Sci. Rep.* **2019**, *9*, 17570.

Recommended by ACS

Glucose-Responsive Chitosan Nanoparticle/Poly(vinyl alcohol) Hydrogels for Sustained Insulin Release *In Vivo*

Akbar Ali, Suchetan Pal, *et al.*

JUNE 27, 2023

ACS APPLIED MATERIALS & INTERFACES

READ 

Bioinspired pH-Responsive Microalgal Hydrogels for Oral Insulin Delivery with Both Hypoglycemic and Insulin Sensitizing Effects

Chaojie Ren, Min Zhou, *et al.*

JULY 05, 2023

ACS NANO

READ 

Hyaluronic Acid-Modified ZIF-8 Nano-Vehicle for Self-Adaption Release of Curcumin for the Treatment of Burns

Xiaoxia Wang, Jinlong Ma, *et al.*

NOVEMBER 02, 2022

ACS APPLIED NANO MATERIALS

READ 

Polymeric Microneedle Arrays with Glucose-Sensing Dynamic-Covalent Bonding for Insulin Delivery

Zhou Ye, Matthew J. Webber, *et al.*

SEPTEMBER 29, 2022

BIOMACROMOLECULES

READ 

Get More Suggestions >

Multifaceted Carbon Dots: toward pH-Responsive Delivery of 5-Fluorouracil for In Vitro Antiproliferative Activity

Navpreet Kaur,¹ Pranav Tiwari,¹ Pawan Kumar, Mainak Biswas, Avinash Sonawane, and Shaikh M. Mobin*



Cite This: *ACS Appl. Bio Mater.* 2023, 6, 2760–2770



Read Online

ACCESS |



Metrics & More



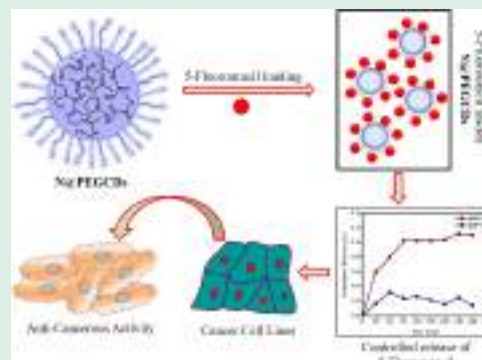
Article Recommendations



Supporting Information

ABSTRACT: The synthesis of smart hybrid material to assimilate diagnosis and treatment is crucial in nanomedicine. Herein, we present a simple and facile method to synthesize multitasking blue-emissive nitrogen-doped carbon dots N@PEGCDs. The as-prepared carbon dots N@PEGCDs show enhanced biocompatibility, small size, high fluorescence, and high quantum yield. The N@PEGCDs are used as a drug carrier for 5-fluorouracil (5-FU) with more release at acidic pH. Furthermore, the mode of action of drug-loaded CD (5FU-N@PEGCDs) has also been explored by performing wound healing assay, DCFDA assay for ROS generation, and Hoechst staining. The drug loaded with carbon dots showed less toxicity to normal cells compared to cancer cells, making it a perfect candidate to be studied for designing next-generation drug delivery systems.

KEYWORDS: carbon dots, biocompatible, nitrogen doping, 5-fluorouracil, drug delivery, anticancer



1. INTRODUCTION

Nanomaterials have been studied extensively in recent years for their outstanding contributions to diagnosis and therapy. Various carbon-based nanomaterials and quantum dots were used extensively for bioimaging, sensing, drug delivery, antibacterial activity, photosensitizer, gene delivery, etc.^{1–6} The carbon dots emerge as a robust candidate for the carbon nanomaterial family and show great potential in theranostics.^{7–9} Since the accidental discovery of carbon dots in 2004, it has been explored for activity in many applications, from optoelectronics, sensing, exfoliation, catalysis, energy storage, and environmental remediation to biomedical applications.^{10–17} The excellent photophysical properties of carbon dots, and their highly biocompatible nature, provide them with a higher position among the nanomaterials. Among all the diseases, cancer leads among the causes of death;¹⁸ many cancer patients are still treated by using conventional chemotherapies. These therapies apart from severe side effects have multiple problems associated with drug toxicity toward normal cells, lesser bioavailability of the drug, drug interaction with other biomolecules, nonspecificity toward a particular type of cancer cells, etc.^{19,20} Various problems associated with chemotherapy can be overcome by using a specially designed drug delivery system.^{21–23} Maximum chemotherapeutic drugs are poorly soluble in water, so getting them entrapped or paired with an aqueous soluble delivery system will enhance their therapeutic efficacy.²⁴

The easy surface functionalization, resistance to photobleaching, and remarkable biocompatibility of carbon dots

always make it interesting to use them as fluorescent probes for bioimaging. Since the discovery of green fluorescent protein (GFP), it has been utilized as a probe to monitor biomolecule interactions, localization, and gene expression.²⁵ However, its inability to resist photobleaching and less fluorescence encourage the researchers to develop other probes to be used successfully in bioimaging. On the contrary, owing to their promising physicochemical properties, the carbon dots are considered a potential candidate as imaging agents. The pristine carbon dots could easily be modified to tune their optical properties and surface functionality for organelle or cell targeting. The highly fluorescent and biocompatible nature of carbon dots is also utilized to prepare in-vivo imaging probes. Since its discovery, multipurpose carbon dots have also been used for sensing metal ions. Since then, the specific, selective, fast, and precise detection of metal ions using carbon dots-based sensors has witnessed a surge.

We demonstrate the synthesis of surface-functionalized nitrogen-doped carbon dots as an effective drug carrier. The as-synthesized carbon dots are reported to act as a carrier of the antimetastatic drug 5-Fluorouracil (5-FU) and exhibited

Received: March 24, 2023

Accepted: June 7, 2023

Published: June 27, 2023



enhanced release in the tumor microenvironment. It helps improve drug efficacy and lessen the side effects on normal cells compared to conventional therapies. Therefore, the N@PEGCDs alone and the association of 5-FU with them can serve as a new platform for bioimaging, sensing, and an intelligent drug delivery system.

2. EXPERIMENTAL SECTION

2.1. Materials and Instruments. The precursors for the synthesis of carbon dots were attained from Sigma-Aldrich. The anions and metal salts were also procured from Sigma-Aldrich and Merck. The chemicals received were of analytical grade, requiring no further purification. The deionized water (DI) obtained from Sartorius milli-Q system was used to perform all the experiments. The X-ray diffraction (XRD) was performed using a Rigaku, RINT 2500 V X-ray diffractometer with Cu K α radiation (1.5406 Å). The Varian Cary 100 Bio UV–visible spectrophotometer was used to perform UV–visible spectroscopic studies. A Fluoromax spectrofluorometer was used to conduct fluorescence studies. IR spectra (4000–400 cm^{−1}) and X-ray photoelectron spectroscopy (XPS) were recorded using Bio-Rad FTS 3000MX instrument and AXIS ULTRA, respectively. TEM images were recorded using a FEI Tecnai G2-F20 Transmission Electron Microscope. The cellular imaging studies were carried out using an Olympus laser scanning microscope. A Synergy H1 Biotek microplate reader was used for absorption studies of MTT assay.

2.2. Synthesis of N@PEGCDs. The hydrothermal carbonization process was drawn to obtain the nitrogen-doped carbon dots (N@PEGCDs). The PEG and trimesic acid were used as carbon precursors and ethylenediamine as nitrogen sources. The PEG is used to attain better cytocompatibility of the synthesized C-dots, whereas nitrogen is doped to enhance the quantum yield (QY) in turn fluorescence of carbon dots. A homogenous PEG and trimesic acid solution were prepared in DI water by sonication for 30 min. In this solution, ethylenediamine was added dropwise and mixed. The whole mixture was poured into a Teflon-coated autoclave vial of 100 mL capacity and placed into a muffle furnace. The furnace was operated at 200 °C for 12 h. The resultant solution was cooled to room temperature, centrifuged at 10,000 rpm for 30 min to remove any large particles, dialyzed (10 kDa) overnight, collected in a clean vial, and kept at room temperature. The obtained solution was lyophilized to remove water. After lyophilization, a light brown sticky material was obtained, which was stored to be re-suspended in DI water to be used hereafter.

2.3. Preparation of 5-FU-Loaded N@PEGCDs. The simple stirring method is followed to load 5-FU on N@PEGCDs. The loading of 5-FU on N@PEGCDs was achieved by adding 800 mg L^{−1} 5-fluorouracil into the aqueous solution of N@PEGCDs. Both ingredients were allowed to react for 24 h by vigorous stirring at room temperature. The unloaded 5-FU was removed by dialyzing the obtained solution using a dialyzing membrane of MWCO 2000Da for 3 h. The 5FU-N@PEGCDs nanocarrier was lyophilized for further characterization using various techniques. The drug loading efficiency (DLE) and drug loading capacity (DLC) were calculated using equation 1.

$$\text{DLE (\%)} = \left[\frac{A_{(T)} - A_{(F)}}{A_{(T)}} \right] \times 100 \quad (1)$$

$A_{(T)}$ is the absorbance of the initially added amount of 5-FU in the solution, $A_{(F)}$ is the unloaded amount of 5-FU, which is calculated by taking the absorbance of the solution outside the dialysis bag after 2 h of dialysis, and $W_{(C)}$ is the total weight of the carrier which is N@PEGCDs added initially.

2.4. In Vitro Release of 5-FU. To check the in vitro release of 5-FU from 5FU-N@PEGCDs, two different pH conditions were evaluated, that is, pH 7.4, which is the physiological pH, and pH 5.4, which is the pH of cancerous tissue. The PBS and acetate buffers were used to achieve these pH conditions. The 5FU-N@PEGCDs system was dialyzed against a buffer of different pHs utilizing a dialysis

membrane of MWCO 2000 Da at 37 °C for 24 h. The 2 mL solution was taken out from the buffer outside the dialysis membrane at regular intervals, and the release of 5-FU was determined using UV–vis spectroscopy. To calculate the percentage of the released drug, eq 2 was used.

$$\begin{aligned} \text{Cumulative release (\%)} \\ = \text{drug released/total loaded drug content} \times 100 \end{aligned} \quad (2)$$

2.5. Cytotoxicity Assay and Bioimaging. To perform the various cell-related experiments, the cells were grown at 37 °C in a 5% CO₂ environment using Dulbecco's modified Eagle medium (DMEM) supplemented with 10% (v/v) FBS (fetal bovine serum) and 1% antibiotics penicillin/streptomycin, 10,000 U mL^{−1}. The A375 (human melanoma cell line) and HEK (human embryonic kidney cell line) were grown and used for cellular studies. The viability of both the cells (A375 and HEK) was checked in the presence of N@PEGCDs, 5FU-N@PEGCDs, and 5-FU by a conventional MTT assay. The cells at the density of 1×10^4 were seeded in 96-well plates and grown for 24 h. Subsequently, the media were replaced by fresh media containing N@PEGCDs, 5FU-N@PEGCDs, and 5-FU. The N@PEGCDs were checked for the concentration ranging from 200 to 1000 $\mu\text{g mL}^{-1}$, whereas the free 5-FU and 5FU-N@PEGCDs were tested for the concentration ranging from 0.25 to 16.0 $\mu\text{g mL}^{-1}$ in triplicates. The wells containing only media were taken as control. After 24 h, the media was replaced with fresh media containing MTT of 5 mg mL^{−1}. The purple-colored formazan crystals were dissolved using 100 μL of DMSO per well, and the absorbance was recorded at 570 nm using a UV-plate reader. The percent cell viability was calculated using eq 3.

$$\% \text{ Cell viability} = \text{Abs}_{(T)} / \text{Abs}_{(C)} \times 100 \quad (3)$$

For bioimaging, A375 cells were grown in confocal dishes for 24 h following the same procedure and under similar conditions described earlier. After 24 h, the grown cells were washed once with PBS and then treated with N@PEGCD (250 $\mu\text{g mL}^{-1}$) for 4 h. To capture the cell images using a confocal microscope, the cells were prepared by first washing with PBS twice and then adding 2 mL of fresh DMEM. The live-cell images were captured using blue and green laser sources (405 and 488).

2.6. Hoechst Staining. The morphological changes in the cells after treatment with N@PEGCDs and 5FU-N@PEGCDs were evaluated using Hoechst stain 33258. The A375 cells were grown in 6-well plate for 24 h. After 24 h, the cells were treated with the corresponding IC₅₀ concentration of N@PEGCDs and 5FU-N@PEGCDs, and 5-FU as a positive control. The cells without any treatment were taken as a negative control. After 24 h of treatment, the cells were washed with PBS and stained using Hoechst stain (5 $\mu\text{g mL}^{-1}$) for 30 min. The images were captured using a blue laser of a confocal microscope.

2.7. In Vitro Scratch Assay. To access the effect of N@PEGCDs and 5FU-N@PEGCDs treatment on cell migration, the A375 cells were grown in 6-well plate until they achieved 100% confluency. These fully confluent wells were wounded using a 200 μL pipette tip. The debris was removed by washing, and fresh media containing IC₅₀ concentrations of N@PEGCDs, 5FU-N@PEGCDs, and 5-FU were added to all the wells. The wounded region was photographed using an inverted microscope at intervals of 0, 12, 24, and 48 h. To obtain a picture of the same point every time, the area was marked on the outer bottom of the dish.

2.8. DCFDA Assay for ROS Generation. 2',7'-Dichlorofluorescein diacetate (DCFDA) assay was performed to check ROS generation. The cells take up DCFDA, which gets oxidized by cellular reactive oxygen species (ROS) to generate fluorescent 2',7'-dichlorofluorescein (DCF) with emission maxima 529 nm. The cells were grown in confocal dishes following the procedure described earlier. After 24 h, the cells were treated with DCFDA (10 μM in DMSO) for 30 min, followed by washing with PBS. A confocal microscope captured images at an excitation of 488 nm, and emission signals were collected in the range of 490–560 nm.

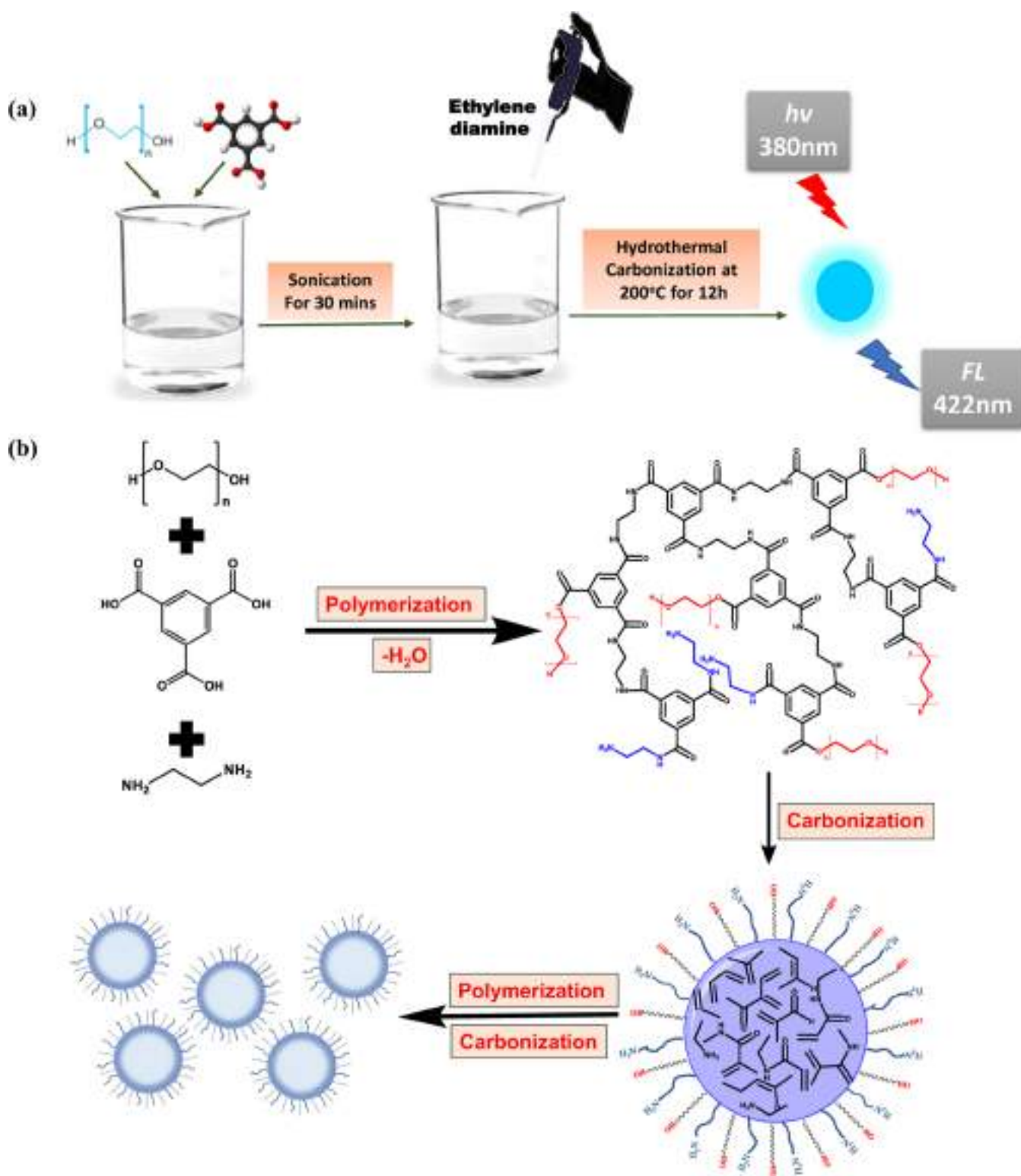


Figure 1. (a) Schematic illustration for synthesis strategy of N@PEGCDs and (b) the probable mechanism involved in the formation of N@PEGCDs.

2.9. Western Blotting. A375 and HEK2 (10^6) cells were seeded in six-well or 60 mm tissue culture plates. Cells were treated with IC₅₀ (Concentration) of N@PEGCDs and 5FU-N@PEGCDs for 24 h. Then, cells were harvested, and protein samples were prepared by cell lysis using 80 to 100 μ L of lysis buffer (1 M Tris, 2 M NaCl, 0.1 M EDTA, 100 mM DTT, 1% Triton X 100, Na₃VO₄·2H₂O, 10% glycerol, and PMSF) supplemented with a protease inhibitor cocktail. Proteins were electrophoresed in 10% SDS-PAGE and transferred to a

PVDF membrane, and then membranes were incubated with primary rabbit anti-PARP and anti-BCL-xL IgG antibodies (dilution 1:3000) overnight at 4 °C followed by secondary goat anti-rabbit antibodies (1:5000) for 2 h at room temperature. All the primary and secondary antibodies were procured from cell-signaling technologies (CST), Massachusetts, US. The membrane was developed using chemiluminescent solvents in the Vilber Fusion SOLO S Gel Doc system. The relative band densities were quantified relative to respective loading

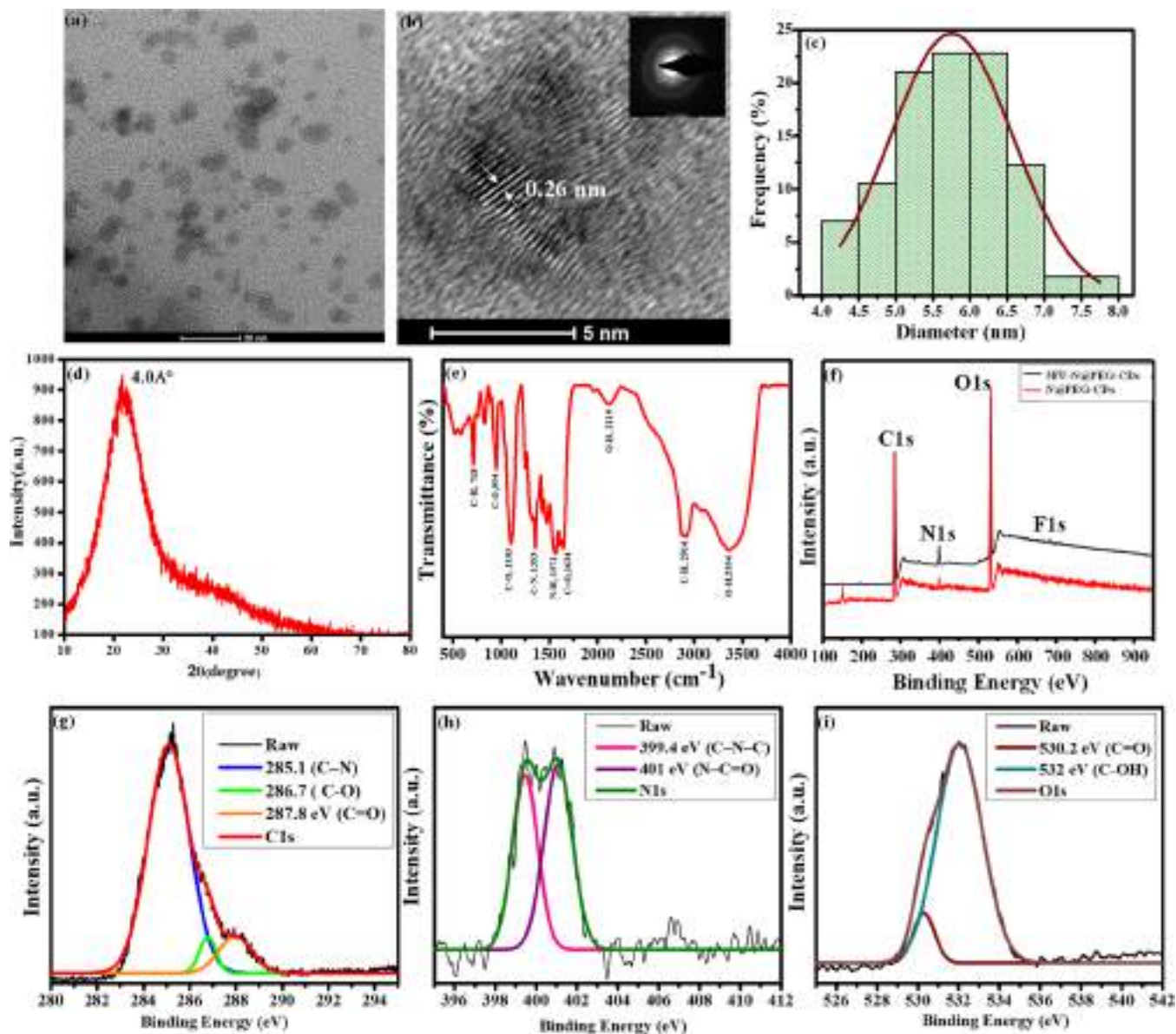


Figure 2. Structural and optical characterization of N@PEGCDs. (a) TEM, (b) HR-TEM, (c) particle size distribution, (d) PXRD, (e) FT-IR, and (f) XPS survey scan of N@PEGCDs and 5FU-N@PEGCDs. XPS high-resolution spectrum for (g) N@PEGCDs: C 1s, (h) N@PEGCDs: N 1s, and (i) N@PEGCDs: O 1s.

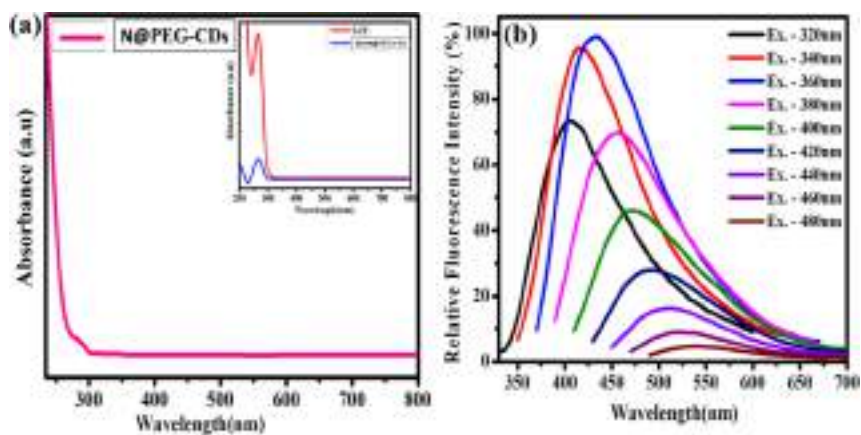


Figure 3. Optical characterization: (a) UV-vis spectra of N@PEGCDs. The UV spectra of 5FU and 5FU-N@PEGCDs (inset) and (b) wavelength-tuned emission of N@PEGCDs.

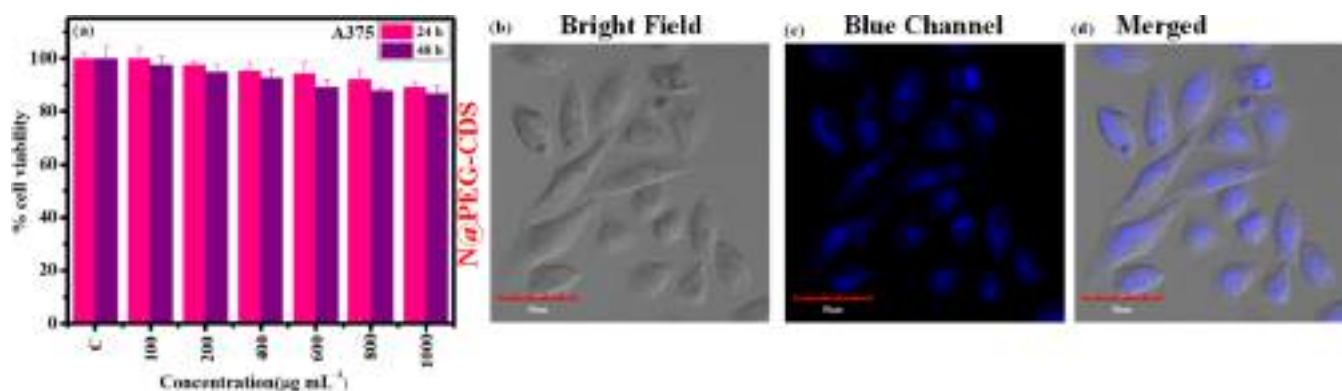


Figure 4. (a) Cytotoxicity assay of N@PEGCDs (100–1000 $\mu\text{g mL}^{-1}$) and (b–d) bioimaging of A375 cells using N@PEGCDs (200 $\mu\text{g mL}^{-1}$) at 37 °C for 6 h.

Scheme 1. Schematic Illustration for Synthesis Strategy of SFU-N@PEGCDs



controls using the ImageJ software (National Institutes of Health, Bethesda, MD, USA).

3. RESULTS AND DISCUSSION

3.1. Preparation and Characterization of N@PEGCD.

The nitrogen-doped carbon dots were obtained using trimesic acid and PEG as carbon sources and ethylenediamine for nitrogen doping *via* the hydrothermal method. Trimesic acid was used due to various functional groups (–OH and –COOH), and PEG is used to impart biocompatibility to the product. Nitrogen doping can enhance QY and bring about divergent surface states to improve the photostability for N@PEGCDs. The hydrothermal treatment was carried out for 12 h at 200 °C to obtain fluorescent N@PEGCDs, as shown in Figure 1a. The light-yellow mixture of precursors turns to brown color after hydrothermal treatment, evincing the formation of carbon dots. The QY of the N@PEGCDs was calculated to be 43%. The enhanced QY is resultant of nitrogen doping.²⁶

To understand the mechanism behind the formation of N@PEGCDs is demonstrated in Figure 1b. The carboxyl group of trimesic acid first polymerizes with an amine of ethylenediamine and a hydroxyl group of PEG to form a polymer through dehydration, which further carbonizes and bursts to produce surface-functionalized fluorescent carbon dots.^{12,27}

3.1.1. Morphological and Structural Characterization of N@PEGCDs. HR-TEM, XPS, FTIR, XRD, and UV–vis spectroscopy were carried out to characterize the formed N@PEGCDs. HR-TEM determined the morphology and size of N@PEGCDs, as shown in Figure 2a. Most particles are spherical with an amorphous structure, which is supported by PXRD as well. A few particles showed clear lattice fringes with a spacing of 0.26 nm (Figure 2b), suggestive of the graphite-like structure of N@PEGCDs.²⁸ The size of CDs calculated from HR-TEM images ranges from 4.5 to 7 nm (Figure 2c).

The SAED pattern shown in Figure 2b (inset) also supports the presence of little crystallinity in otherwise amorphous N@PEGCDs. In PXRD (Figure 2d), the broad hump at $2\theta = 21.8^\circ$ corresponds to the amorphous nature of the material.²⁹ The *d*-spacing was calculated to be 4.0 Å which could be assigned to distorted sp^2 hybridization.³⁰ The functional group present on the surface of N@PEGCDs was studied by FT-IR, as shown in Figure 2e. The broad peak at 3354 cm^{-1} was attributed to the stretching vibration of O–H,³¹ whereas the peak at 2914 cm^{-1} was the antisymmetric stretching of C–H.³² The stretching vibration at 1634 cm^{-1} of C=O and 1103 cm^{-1} of C–O demonstrates oxygen-rich groups on the surface of N@PEGCDs.³³ The bending vibration of N–H²⁹ and C–N³⁴ was exhibited at 1571 and 1353 cm^{-1} . The FT-IR data confirms the presence of amine and nitrogen-rich functionality on the surface of N@PEGCDs. The XPS spectra shown in Figure 2f revealed the presence of two high-intensity peaks at 284.4 and 532.4 eV assigned to C 1s and O 1s, respectively. Another low-intensity peak present at 398.6 suggested the presence of N 1s in the elemental composition of N@PEGCDs. The deconvoluted spectra of C 1s correspond to sp^3 carbon C–N at 285.1 eV, the presence of C–O at 286.7 eV, and C=O at 287.8 eV.^{35–37} The N 1s high-resolution XPS spectra on deconvolution showed two peaks at 399.4 and 401 eV, denoting porphyrin C–N–C and aromatic N–C=O, respectively.^{38,39} In high-resolution spectra of O 1s, the two peaks at 530.2 and 532 eV were ascribed to C=O and C–OH.⁴⁰ The high-resolution spectra of C 1s, N 1s, and O 1s are shown in Figure 2g–i.

To determine the photophysical properties of N@PEGCDs, the UV–vis spectrum of N@PEGCDs was performed (Figure 3a), which reveals the presence of a shoulder at 286 nm attributed to the π – π^* transition of C=C and C=N. Here, the carbonyl and carboxyl groups are assumed to be present on the surface of N@PEGCDs; however, the C=C originated

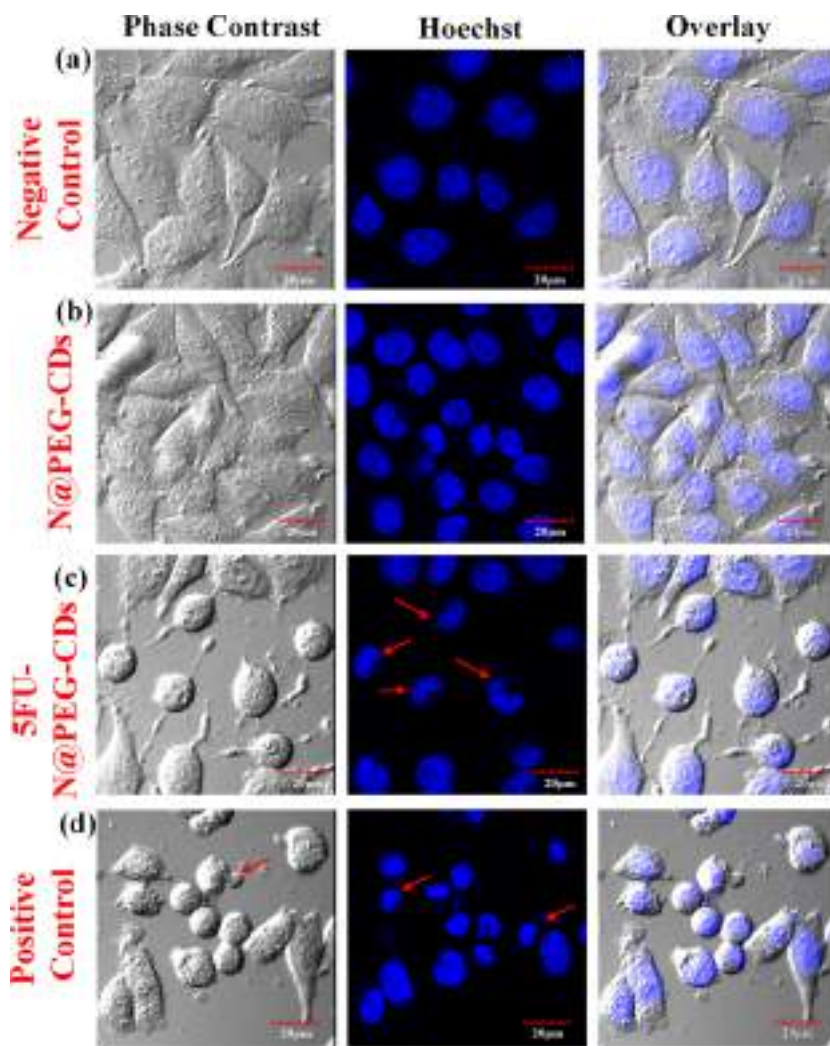


Figure 5. Confocal microscopic analysis of A375 cells treated with (a) negative controls, (b) N@PEGCDs, (c) 5FU-N@PEGCDs, and (d) positive controls.

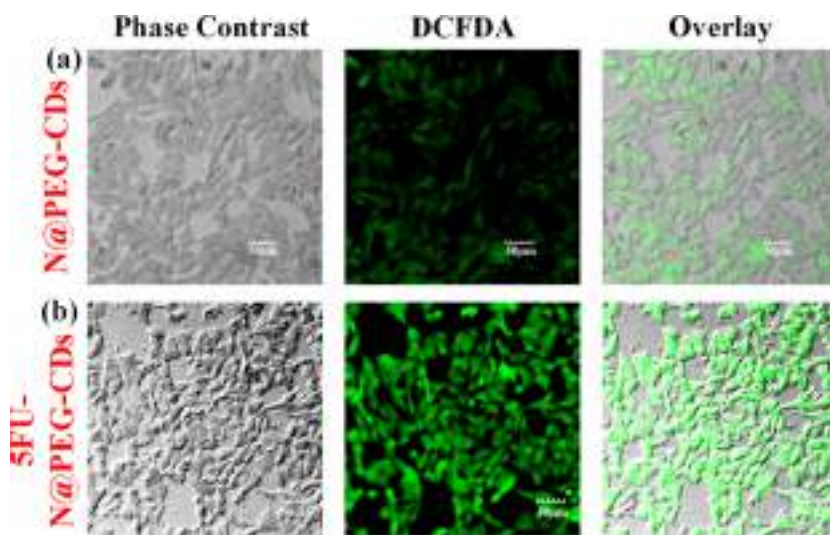


Figure 6. Confocal images of A375 cells after treatment with (a) N@PEGCDs and (b) 5FU-N@PEGCDs and stained with DCFDA.

from the polymeric domains situated at the core with sp^2 hybridization.⁴¹ The different surface states of N@PEGCDs are also a reason for this shoulder in the near-visible region.⁴²

The various functional groups present on the surface of N@PEGCDs make it a promising candidate to be used in multiple applications in different areas. Further, fluorescence spectroscopy

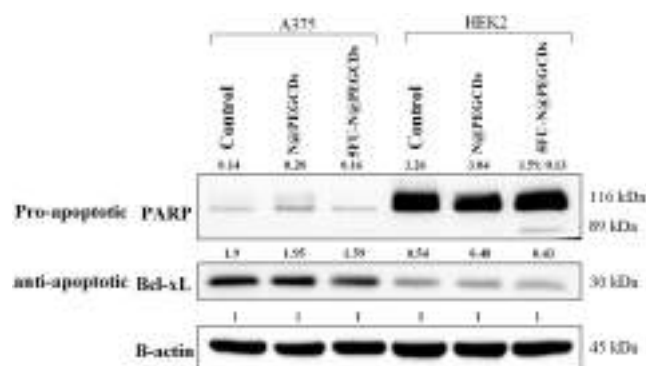


Figure 7. Western blot using protein extracted from A375 cells after treatment with N@PEGCDs and 5FU-N@PEGCDs.

copy was performed for N@PEGCDs. The results shown in Figure 3b indicate the excitation-dependent emission behavior of N@PEGCDs. N@PEGCDs showed maximum emission at 440 nm with the excitation wavelength of 360 nm. This behavior could be explained due to different surface states, polydispersity, carbon dot mixture, or the formation of aggregates.^{43,44}

3.2. Biocompatibility and Bioimaging Using N@PEGCDs. After excellent photophysical properties, the biocompatibility of N@PEGCDs was estimated using A375 (melanoma cancer cell line) up to 48 h by treating with concentrations ranging from 100 to 1000 $\mu\text{g mL}^{-1}$. The results shown in Figure 4a suggest the favorable biocompatible nature of N@PEGCDs. There is more than 85% cell viability even after 48 h. The outstanding biocompatibility and admirable optical properties make it a favorable fluorescent probe to be used as a bioimaging agent. On excitation with a blue laser of wavelength 405 nm, cells show blue fluorescence coming from the cytoplasmic region as shown in figure 4b–d. It is important to mention here that the N@PEGCDs are found to be highly hemocompatible too (Figure S1). Moreover, the fluorescence stability of as-prepared N@PEGCDs was assessed at different

conditions, as shown in Figures S2 and S3. To start with, N@PEGCDs were incubated at different temperatures, pHs, and in the presence of UV and no significant change in fluorescence was observed, suggesting that carbon dot colloidal dispersion was well stabilized and does not get degraded. Moreover, since the major use of the prepared carbon dots was in cellular studies, the stability of N@PEGCDs was also checked in biological media at different incubation periods. As shown in Figures S2d and S3, the fluorescence of N@PEGCDs does not get fluctuated much, suggesting that most of the colloidal dispersion were stabilized with the biological media and thus taking part in the biological studies. Apart from checking the stability of N@PEGCDs, its cellular uptake was also studied, as shown in Figure 4b–d. After the uptake of N@PEGCDs, cells exhibited blue fluorescence which was coming from the N@PEGCDs. Also, the cellular morphology was well preserved further supporting the biocompatible nature of N@PEGCDs.

3.3. Synthesis of 5FU-N@PEGCDs, Characterization, and Drug Loading Study. Carbon dots are having various surface functionalities. These provide carbon dots an additional advantage over other nanomaterials for getting conjugated easily with drugs, biomolecules, or other chemical compounds. The N@PEGCDs were chosen as a carrier for delivery of anticancer drug 5-FU due to the possession of multiple functionalities proven by FTIR and XPS earlier. It must be mentioned that N@PEGCDs and 5-FU both exhibited negative charge value as calculated from zeta potential measurement, i.e., -8.56 and -16.7 mV and after loading of 5-FU with the prepared CD, the zeta potential value was -23.7 mV, the negative zeta potential value suggested that the interaction is non-electrostatic and possibly occurred between the different functional groups present in 5-FU and N@PEGCDs. The FTIR spectrum of N@PEGCDs and 5-FU as shown in Figure S4 showed prominent peaks corresponding to N–H stretching, C–H, C=O, and so forth, whereas after conjugation, shifting in FTIR band was observed. The obtained FTIR spectrum suggest hydrogen bonding between

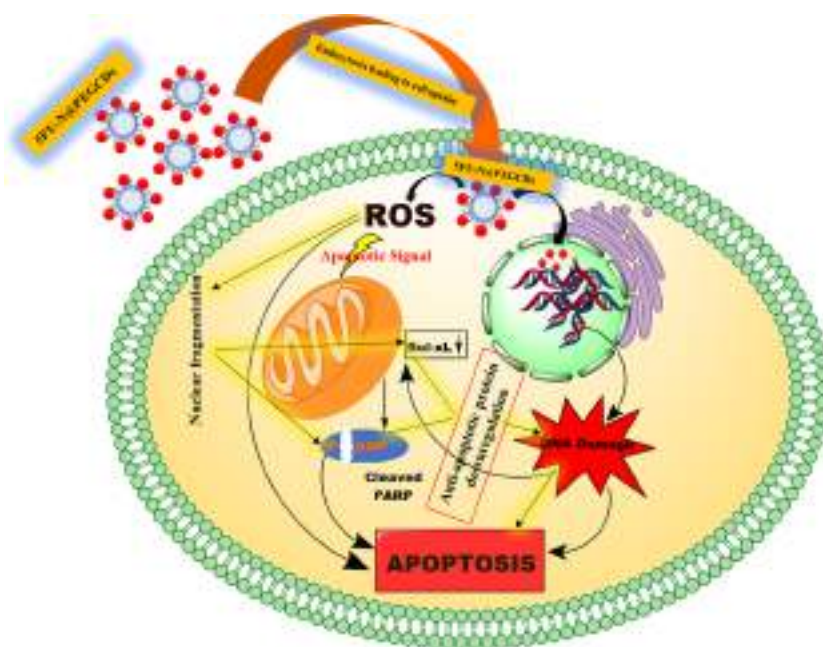


Figure 8. Mechanism of cell death by using drug-loaded carbon dots.

C—O and N—H groups of 5-FU and —OH and —NH₂ groups of N@PEGCDs. Also, since 5-FU contains double C=C bond, thus it can also bind with N@PEGCDs through π – π interactions.^{45,46} TEM images of SFU-N@PEGCDs showed similar morphology and size-like N@PEGCDs, as shown in Figure S5a,b, which was further supported by the PXRD spectrum of SFU-N@PEGCDs, as shown in Figure S6. Even after loading 5-FU drug in N@PEGCDs, the formed nanocarrier exhibited similar spectrum like N@PEGCDs. The DLE was calculated to be 52.3% and were compared with the earlier published works, as shown in Table S1. It is believed that the functional group present on the surface of N@PEGCDs makes it a desirable candidate to interact easily with 5-FU. The synthesis procedure is shown in Scheme 1.

The inset of Figure 3a shows UV–vis spectra of SFU-N@PEGCDs along with only 5-FU. SFU-N@PEGCDs, N@PEGCDs, and 5-FU display a clear peak at 266 nm, which is the characteristic peak of 5-FU, supporting the fact that 5-FU has been loaded successfully on N@PEGCDs. The successful loading of 5-FU with N@PEGCDs is also confirmed by XPS spectra of the SFU-N@PEGCDs, as shown in Figure 2f. The peak at 683.5 eV was assigned to F 1s.⁴⁷ Apart from UV–vis and XPS, PXRD was also performed of SFU-N@PEGCDs and compared with 5-FU drug and N@PEGCDs.

3.4. In Vitro Drug Release Profile, Cytotoxicity, Hemocompatibility, and Anticancer Activity of SFU-N@PEGCDs. Any material used as a drug carrier should have a few qualities such as reduced cytotoxicity, controlled drug release, real-time monitoring, and stimulus-responsive delivery. To check the ability of SFU-N@PEGCDs to act as a drug delivery system, the drug release profile was studied at two different pHs, one is 7.4, physiological pH, and another is 5.4, pH around cancerous tumors (Figure S7a). The cumulative release of 5-FU is higher at lower pH than the physiological pH. This gives the SFU-N@PEGCDs delivery system the advantage of releasing more drugs around the tumor microenvironment. In addition, it could be inferred that the delivery of the antineoplastic drug is in the presence of external stimuli, i.e., a change in pH.

The biocompatible nature of N@PEGCDs is already discussed earlier. The biocompatibility of SFU-N@PEGCDs has also been studied in HEK (human embryonic kidney cells), a standard cell line, and A375 (melanoma cells), a cancerous cell line for 24 h (Figure S7b,c). The free 5-FU was also used to determine the effect of loading on the cytotoxicity profile of the drug. The cell viability declines in normal and cancerous cells with free 5-FU and SFU-N@PEGCDs nanocarrier treatment. However, the toxicity of the free drug is more toward normal cells than SFU-N@PEGCDs. At the highest treatment concentration of 8 $\mu\text{g mL}^{-1}$, 20% of the cells treated with free 5-FU is viable, while the viability of SFU-N@PEGCDs treated cells is 30%. In contrast, when the cancerous cells are treated with equivalent concentrations of free and loaded drugs, the viability follows dose-dependent behavior. The drug loaded with carbon dots kills more cancerous cells than the free drug. The equivalent concentration of both free and loaded drugs kills approximately 70 and 80% of cells. The results also confirm that the loading of 5-FU with N@PEGCDs does not alter its activity. This proposes the substantial prospective of SFU-N@PEGCDs in cancer treatment because its reduced cytotoxicity toward normal cells results in decreased adverse effects on patients hence better tolerance to the drug throughout the course of treatment.

3.5. Cellular Interactions and Mode of Action of SFU-N@PEGCDs. It is evident from the previous results that N@PEGCDs were taken up by the cells. Therefore, SFU-N@PEGCDs could also be taken up by cells and 5-FU gets released inside the cells to kill it or, the drug gets released from SFU-N@PEGCDs at the tumor site and taken up by cells which kills the cells. In any case, the mode of action of SFU-N@PEGCDs for killing the cell was studied through various assays. The 5-FU gets intruded into nucleoside metabolism and gets incorporated into cellular DNA or RNA, leading to the initiation of the apoptotic pathway to ultimately kill cell.⁴⁸ The signs of morphological changes in nuclei, blebbing, chromatin fragmentation or condensation, and bi- or multi-nucleation were investigated by Hoechst staining. The A375 cells after treatment with IC₅₀ values of SFU-N@PEGCDs for 24 h were stained with Hoechst (Figure 5). The nucleus of nontreated cells and cells treated with N@PEGCDs is evenly stained, while the SFU-N@PEGCDs treated cells show a change in nucleus morphology. Their condensed and fragmented chromatin, cytoplasmic blebbing, and multi-nucleation are comparable to positive control.

Reduced cell migration is another measure chosen to check the antiproliferative action of any drug or complex. The cell migration assay/wound healing assay was carried out on the A375 cells as described earlier. The cancer cells invade neighboring tissues through migration which occurs due to the action of many genes.⁴⁹ Many anticancerous drugs target these genes to inhibit the spread of metastatic cells from one organ to another. Figure S8 depicts the delayed wound closure in the cells treated with SFU-N@PEGCDs. In negative control and N@PEGCDs, treated wounds heal almost 100% after 48 h, while approximately 45% of the wounded area remains wounded in SFU-N@PEGCDs-treated cells. Therefore, it could be inferred that the SFU-N@PEGCDs suppress cell migration considerably.

Chemotherapy often leads to the formation of ROS, which could cause cell death through apoptosis. The treatment of cells with SFU-N@PEGCDs can also generate ROS in the treated cells. The generated ROS was determined by DCFDA assay. The enhancement of fluorescence in the treated cell is a clear indication of the presence of ROS, as shown in Figure 6. It further supports the assumption of cell death by apoptosis after SFU-N@PEGCDs treatment.

To dissect the apoptotic signaling pathway, we investigated the effects of N@PEGCDs and SFU-N@PEGCDs on apoptotic proteins in A375 and HEK cell lines by Western blotting. The apoptotic mitochondrial events are regulated by members of the Bcl-2 family of proteins.⁵⁰ Antiapoptotic protein Bcl-XL is a member of the Bcl-2 family. It is a major transmembrane molecule of mitochondria that prevents apoptosis by blocking the release of mitochondrial contents like cytochrome *c* into cytosol; therefore, its expression was expected to be downregulated in apoptotic cells. As anticipated, the expression of antiapoptotic protein Bcl-XL was downregulated in SFU-N@PEGCDs-treated cells (Figure 7.). Next, we investigated the effects of N@PEGCDs and SFU-N@PEGCDs on a proapoptotic protein poly (ADP-ribose) polymerase (PARP), which is involved in the repair of DNA damage. Therefore, cleavage of PARP by caspase-3 will inhibit the DNA repair mechanism leading to apoptosis.⁵¹ Apoptosis was induced by exposing the cells to SFU-N@PEGCDs treatment and confirmed by observing the cleavage of the PARP molecule to the characteristic 89 kDa C-terminal

fragment. Together these results suggest that 5FU-N@PEGCDs induce PARP-mediated apoptosis. The enhanced release of cytochrome *c* in 5FU-N@PEGCDs was also checked which also supports the apoptotic cell death (Figure S9).

3.6. Cell Death Mechanism. The results herein demonstrated bring forth insights into cell death by apoptosis. The carbon dots loaded with 5-FU are internalized to the cell by endocytosis. The drug release led to DNA damage, nuclear fragmentation, and ROS generation, activating the apoptotic signaling pathway.^{52,53} The apoptotic signals activate specific genes to cause cell death. The downregulation of BCL-xL could no longer prevent the release of mitochondrial content into the cytoplasm hence apoptosis.⁵⁴ The cleaved PARP prevents DNA repair, which is again a favorable factor in apoptosis.^{55,56} The whole mechanism of cell death by apoptosis is summarized diagrammatically in Figure 8.

4. CONCLUSIONS

In this work, the facile preparation of nitrogen-doped carbon dots (N@PEGCDs) and a unique drug delivery system formulated by self-assembly of antimetastatic drug 5-FU on the surface of carbon dots are illustrated. The electrostatic interaction of 5-FU with N@PEGCDs made it less toxic to normal cells than a free drug, resulting in better drug tolerance. The mechanism behind the cell death caused by 5FU-N@PEGCDs precisely indicates ROS's role, nuclear changes, and downregulation of antiapoptotic and upregulation of proapoptotic factors in apoptosis. The detailed mechanism of action is notable for future studies. Furthermore, the biocompatible N@PEGCDs were characterized thoroughly and were used as a fluorescent bioimaging probe. The results will expedite the growth of carbon dots for their application in theranostics. The present work offers a great possibility of OD fluorescent carbon nanomaterials for drug delivery applications, which in future can be extended for gene delivery too. The results obtained are very promising, and further systematic studies are needed to fully explore its translational potential. The N@PEGCDs were cytocompatible, and further detailed studies especially its biodistribution and elimination pathway are needed to be studied. Later ex vivo and animal studies can provide the targeting capability of N@PEGCDs which is very much essential for its translational applications.

■ ASSOCIATED CONTENT

SI Supporting Information

The Supporting Information is available free of charge at <https://pubs.acs.org/doi/10.1021/acsabm.3c00228>.

Instrument details; calculation of QY; hemolytic assay; release of cytochrome *c*; hemocompatibility of N@PEGCDs; stability of N@PEGCDs; stability of N@PEGCDs in biological media at different incubation periods; FTIR spectrum of 5-FU, N@PEGCDs, and 5FU-N@PEGCDs; TEM images of 5FU-N@PEGCDs; PXRD spectrum of 5-FU, N@PEGCDs, and 5FU-N@PEGCDs; in vitro release profile of 5-FU from 5FU-N@PEGCDs nanoconjugate in different pH values, cytotoxicity results of free 5-FU and 5FU-N@PEGCDs to HEK cells, and A375 cells at different concentrations for 24 h; the scratch test assay with the treatment of N@PEGCDs and 5FU-N@PEGCDs and graphical representation of % wound area remains from close at 0–48

h; cytochrome *c* release; and comparison of 5-FU delivery systems (PDF)

■ AUTHOR INFORMATION

Corresponding Author

Shaikh M. Mobin — Discipline of Biosciences and Bio-Medical Engineering, Indian Institute of Technology Indore, Indore 453552, India; Discipline of Metallurgy Engineering and Materials Science and Discipline of Chemistry, Indian Institute of Technology Indore, Indore 453552, India; orcid.org/0000-0003-1940-3822; Phone: +91-731-2438752; Email: xray@iiti.ac.in

Authors

Navpreet Kaur — Discipline of Biosciences and Bio-Medical Engineering, Indian Institute of Technology Indore, Indore 453552, India

Pranav Tiwari — Discipline of Metallurgy Engineering and Materials Science, Indian Institute of Technology Indore, Indore 453552, India

Pawan Kumar — Discipline of Chemistry, Indian Institute of Technology Indore, Indore 453552, India

Mainak Biswas — School of Biotechnology, KIIT Deemed to be University, Bhubaneswar 751024 Odisha, India

Avinash Sonawane — Discipline of Biosciences and Bio-Medical Engineering, Indian Institute of Technology Indore, Indore 453552, India

Complete contact information is available at: <https://pubs.acs.org/doi/10.1021/acsabm.3c00228>

Author Contributions

[†]N.K. and P.T. have contributed equally.

Notes

The authors declare no competing financial interest.

■ ACKNOWLEDGMENTS

The authors acknowledge Sophisticated Instrumentation Centre, IIT Indore, for all the characterization facilities. N.K. would like to thank UGC, New Delhi, for the research fellowship. P.T. thanks BRNS, and P.K. and M.B. thank MHRD for the fellowship. S.M.M. thanks BRNS (project no. 58/14/17/2020-BRNS/37215), SERB (CRG/2020/001769), and IIT Indore for the financial support. A.S. thanks IIT Indore for the financial support. Sophisticated Instrumentation Centre, IIT Indore, for all the characterization facilities, MNIT-MRC for the XPS facility, SAIF, IITB for the TEM facility, and FTIR facility are gratefully acknowledged.

■ REFERENCES

- (1) Jaleel, J. A.; Pramod, K. Artful and Multifaceted Applications of Carbon Dot in Biomedicine. *J. Controlled Release* **2018**, *269*, 302–321.
- (2) Guo, Y.; Shen, M.; Shi, X. Construction of Poly(Amidoamine) Dendrimer/Carbon Dot Nanohybrids for Biomedical Applications. *Macromol. Biosci.* **2021**, *21*, 2100007.
- (3) Yang, J.; Zhang, X.; Ma, Y.-H.; Gao, G.; Chen, X.; Jia, H.-R.; Li, Y.-H.; Chen, Z.; Wu, F.-G. Carbon Dot-Based Platform for Simultaneous Bacterial Distinguishment and Antibacterial Applications. *ACS Appl. Mater. Interfaces* **2016**, *8*, 32170–32181.
- (4) Kaur, N.; Tiwari, P.; Mate, N.; Sharma, V.; Mobin, S. M. Photoactivatable Carbon Dots as a Label-Free Fluorescent Probe for Picric Acid Detection and Light-Induced Bacterial Inactivation. *J. Photochem. Photobiol., B* **2022**, *229*, 112412.

- (5) Li, H.; Yan, X.; Qiao, S.; Lu, G.; Su, X. Yellow-Emissive Carbon Dot-Based Optical Sensing Platforms: Cell Imaging and Analytical Applications for Biocatalytic Reactions. *ACS Appl. Mater. Interfaces* **2018**, *10*, 7737–7744.
- (6) Tufani, A.; Qureshi, A.; Niazi, J. H. Iron Oxide Nanoparticles Based Magnetic Luminescent Quantum Dots (MQDs) Synthesis and Biomedical/Biological Applications: A Review. *Mater. Sci. Eng., C* **2021**, *118*, 111545.
- (7) Hassan, M.; Gomes, V. G.; Dehghani, A.; Ardekani, S. M. Engineering Carbon Quantum Dots for Photomediated Theranostics. *Nano Res.* **2018**, *11*, 1–41.
- (8) Du, J.; Xu, N.; Fan, J.; Sun, W.; Peng, X. Carbon Dots for In Vivo Bioimaging and Theranostics. *Small* **2019**, *15*, 1805087.
- (9) Lin, J.-S.; Tsai, Y.-W.; Dehvari, K.; Huang, C.-C.; Chang, J.-Y. A Carbon Dot Based Theranostic Platform for Dual-Modal Imaging and Free Radical Scavenging. *Nanoscale* **2019**, *11*, 20917–20931.
- (10) Tiwari, P.; Kaur, N.; Sharma, V.; Kang, H.; Uddin, J.; Mobin, S. M. Cannabis Sativa-Derived Carbon Dots Co-Doped with N-S: Highly Efficient Nanosensors for Temperature and Vitamin B12. *New J. Chem.* **2019**, *43*, 17058–17068.
- (11) Xu, X.; Ray, R.; Gu, Y.; Ploehn, H. J.; Gearheart, L.; Raker, K.; Scrivens, W. A. Electrophoretic Analysis and Purification of Fluorescent Single-Walled Carbon Nanotube Fragments. *J. Am. Chem. Soc.* **2004**, *126*, 12736–12737.
- (12) Sharma, V.; Kaur, N.; Tiwari, P.; Saini, A. K.; Mobin, S. M. Multifunctional Fluorescent “Off-On-Off” Nanosensor for Au³⁺ and S²⁻ Employing N-S Co-Doped Carbon-Dots. *Carbon* **2018**, *139*, 393–403.
- (13) Hola, K.; Zhang, Y.; Wang, Y.; Giannelis, E. P.; Zboril, R.; Rogach, A. L. Carbon Dots—Emerging Light Emitters for Bioimaging, Cancer Therapy and Optoelectronics. *Nano Today* **2014**, *9*, 590–603.
- (14) Sharma, V.; Kaur, N.; Tiwari, P.; Mobin, S. M. Full Color Emitting Fluorescent Carbon Material as Reversible PH Sensor with Multicolor Live Cell Imaging. *J. Photochem. Photobiol., B* **2018**, *182*, 137–145.
- (15) Hu, C.; Li, M.; Qiu, J.; Sun, Y.-P. Design and Fabrication of Carbon Dots for Energy Conversion and Storage. *Chem. Soc. Rev.* **2019**, *48*, 2315–2337.
- (16) Sharma, V.; Tiwari, P.; Kaur, N.; Mobin, S. M. Optical Nanosensors Based on Fluorescent Carbon Dots for the Detection of Water Contaminants: A Review. *Environ. Chem. Lett.* **2021**, *19*, 3229–3241.
- (17) Tiwari, P.; Sharma, V.; Kaur, N.; Ahmad, K.; Mobin, S. M. Sustainable Graphene Production: New Insights into Cannabis Sativa Engineered Carbon Dots Based Exfoliating Agent for Facile Production of Graphene. *ACS Sustainable Chem. Eng.* **2019**, *7*, 11500–11510.
- (18) World Health Organization *World Health Statistics 2018: Monitoring Health for the SDGs, Sustainable Development Goals*; World Health Organization: Geneva, 2018.
- (19) Zimmermann, S.; Dziadziuszko, R.; Peters, S. Indications and Limitations of Chemotherapy and Targeted Agents in Non-Small Cell Lung Cancer Brain Metastases. *Cancer Treat. Rev.* **2014**, *40*, 716–722.
- (20) Behi, M.; Gholami, L.; Naficy, S.; Palomba, S.; Dehghani, F. Carbon Dots: A Novel Platform for Biomedical Applications. *Nanoscale Adv.* **2022**, *4*, 353–376.
- (21) Liu, Z.; Chen, K.; Davis, C.; Sherlock, S.; Cao, Q.; Chen, X.; Dai, H. Drug Delivery with Carbon Nanotubes for In Vivo Cancer Treatment. *Cancer Res.* **2008**, *68*, 6652–6660.
- (22) Wang, Q.; Huang, X.; Long, Y.; Wang, X.; Zhang, H.; Zhu, R.; Liang, L.; Teng, P.; Zheng, H. Hollow Luminescent Carbon Dots for Drug Delivery. *Carbon* **2013**, *59*, 192–199.
- (23) Zavareh, H. S.; Pourmadadi, M.; Moradi, A.; Yazdian, F.; Omid, M. Chitosan/Carbon Quantum Dot/Aptamer Complex as a Potential Anticancer Drug Delivery System towards the Release of 5-Fluorouracil. *Int. J. Biol. Macromol.* **2020**, *165*, 1422–1430.
- (24) Wan, J.; Zhang, X.; Fu, K.; Zhang, X.; Shang, L.; Su, Z. Highly Fluorescent Carbon Dots as Novel Theranostic Agents for Biomedical Applications. *Nanoscale* **2021**, *13*, 17236–17253.
- (25) Li, Z.; Lin, H.; Ding, S.; Ling, H.; Wang, T.; Miao, Z.; Zhang, M.; Meng, A.; Li, Q. Synthesis and Enhanced Electromagnetic Wave Absorption Performances of Fe₃O₄@C Decorated Walnut Shell-Derived Porous Carbon. *Carbon* **2020**, *167*, 148–159.
- (26) Tiwari, P.; Kaur, N.; Sharma, V.; Mobin, S. M. A Spectroscopic Investigation of Carbon Dots and Its Reduced State towards Fluorescence Performance. *J. Photochem. Photobiol., A* **2020**, *403*, 112847.
- (27) Yang, L.; Jiang, W.; Qiu, L.; Jiang, X.; Zuo, D.; Wang, D.; Yang, L. One Pot Synthesis of Highly Luminescent Polyethylene Glycol Anchored Carbon Dots Functionalized with a Nuclear Localization Signal Peptide for Cell Nucleus Imaging. *Nanoscale* **2015**, *7*, 6104–6113.
- (28) Huang, J. J.; Zhong, Z. F.; Rong, M. Z.; Zhou, X.; Chen, X. D.; Zhang, M. Q. An Easy Approach of Preparing Strongly Luminescent Carbon Dots and Their Polymer Based Composites for Enhancing Solar Cell Efficiency. *Carbon* **2014**, *70*, 190–198.
- (29) Li, F.; Liu, C.; Yang, J.; Wang, Z.; Liu, W.; Tian, F. Mg/N Double Doping Strategy to Fabricate Extremely High Luminescent Carbon Dots for Bioimaging. *RSC Adv.* **2014**, *4*, 3201–3205.
- (30) Kaur, N.; Sharma, V.; Tiwari, P.; Saini, A. K.; Mobin, S. M. Vigna Radiata” Based Green C-Dots: Photo-Triggered Theranostics, Fluorescent Sensor for Extracellular and Intracellular Iron (III) and Multicolor Live Cell Imaging Probe. *Sens. Actuators, B* **2019**, *291*, 275–286.
- (31) Lin, F.; Li, C.; Chen, Z. Exopolysaccharide-Derived Carbon Dots for Microbial Viability Assessment. *Front. Microbiol.* **2018**, *9*, 2697.
- (32) Li, L.; Liao, L.; Ding, Y.; Zeng, H. Dithizone-Etched CdTe Nanoparticles-Based Fluorescence Sensor for the off-on Detection of Cadmium Ion in Aqueous Media. *RSC Adv.* **2017**, *7*, 10361–10368.
- (33) Guo, Q.; Luo, H.; Zhang, J.; Ruan, Q.; Prakash Periasamy, A.; Fang, Y.; Xie, Z.; Li, X.; Wang, X.; Tang, J.; Briscoe, J.; Titirici, M.; Jorge, A. B. The Role of Carbon Dots – Derived Underlayer in Hematite Photoanodes. *Nanoscale* **2020**, *12*, 20220–20229.
- (34) Nie, Y.; Guo, J.; Deng, Y.; Weng, W. Synthesis and Application of Fluorescent N,S Co-Doped Carbon Dots Based on on-off-on Quenching Mode for the Collaboration Detection of Iron Ions and Ascorbic Acid. *J. Saudi Chem. Soc.* **2020**, *24*, 865–873.
- (35) Wang, Y.; Su, Q.; Yang, X. Exploration of the Synthesis of Three Types of Multicolor Carbon Dot Originating from Isomers. *Chem. Commun.* **2018**, *54*, 11312–11315.
- (36) Wang, J.; Wei, J.; Su, S.; Qiu, J. Novel Fluorescence Resonance Energy Transfer Optical Sensors for Vitamin B 12 Detection Using Thermally Reduced Carbon Dots. *New J. Chem.* **2015**, *39*, 501–507.
- (37) Dey, D.; Bhattacharya, T.; Majumdar, B.; Mandani, S.; Sharma, B.; Sarma, K. Carbon Dot Reduced Palladium Nanoparticles as Active Catalysts for Carbon–Carbon Bond Formation. *Dalton Trans.* **2013**, *42*, 13821–13825.
- (38) Wu, P.; Li, W.; Wu, Q.; Liu, Y.; Liu, S. Hydrothermal Synthesis of Nitrogen-Doped Carbon Quantum Dots from Microcrystalline Cellulose for the Detection of Fe³⁺ Ions in an Acidic Environment. *RSC Adv.* **2017**, *7*, 44144–44153.
- (39) Ding, Y.; Zhang, F.; Xu, J.; Miao, Y.; Yang, Y.; Liu, X.; Xu, B. Synthesis of Short-Chain Passivated Carbon Quantum Dots as the Light Emitting Layer towards Electroluminescence. *RSC Adv.* **2017**, *7*, 28754–28762.
- (40) Pan, J.; Sheng, Y.; Zhang, J.; Wei, J.; Huang, P.; Zhang, X.; Feng, B. Preparation of Carbon Quantum Dots/TiO₂ Nanotubes Composites and Their Visible Light Catalytic Applications. *J. Mater. Chem. A* **2014**, *2*, 18082–18086.
- (41) Konar, S.; Kumar, B. P.; Mahto, M. K.; Samanta, D.; Shaik, M. A. S.; Shaw, M.; Mandal, M.; Pathak, A. N-Doped Carbon Dot as Fluorescent Probe for Detection of Cysteine and Multicolor Cell Imaging. *Sens. Actuators, B* **2019**, *286*, 77–85.

(42) Cutrim, E. S. M.; Vale, A. A. M.; Manzani, D.; Barud, H. S.; Rodríguez-Castellón, E.; Santos, A. P. S. A.; Alcântara, A. C. S. Preparation, Characterization and in Vitro Anticancer Performance of Nanoconjugate Based on Carbon Quantum Dots and 5-Fluorouracil. *Mater. Sci. Eng., C* **2021**, *120*, 111781.

(43) Ding, H.; Ji, Y.; Wei, J.-S.; Gao, Q.-Y.; Zhou, Z.-Y.; Xiong, H.-M. Facile Synthesis of Red-Emitting Carbon Dots from Pulp-Free Lemon Juice for Bioimaging. *J. Mater. Chem. B* **2017**, *5*, S272–S277.

(44) Liu, H.; Zhao, X.; Wang, F.; Wang, Y.; Guo, L.; Mei, J.; Tian, C.; Yang, X.; Zhao, D. High-Efficient Excitation-Independent Blue Luminescent Carbon Dots. *Nanoscale Res. Lett.* **2017**, *12*, 399.

(45) Horo, H.; Saha, M.; Das, H.; Mandal, B.; Kundu, L. M. Synthesis of Highly Fluorescent, Amine-Functionalized Carbon Dots from Biotin-Modified Chitosan and Silk-Fibroin Blend for Target-Specific Delivery of Antitumor Agents. *Carbohydr. Polym.* **2022**, *277*, 118862.

(46) Miralinaghi, P.; Kashani, P.; Moniri, E.; Miralinaghi, M. Non-Linear Kinetic, Equilibrium, and Thermodynamic Studies of 5-Fluorouracil Adsorption onto Chitosan-Functionalized Graphene Oxide. *Mater. Res. Express* **2019**, *6*, 065305.

(47) Goddeti, K. C.; Kim, S. M.; Lee, Y. K.; Kim, S. H.; Park, J. Y. Chemical Doping of TiO₂ with Nitrogen and Fluorine and Its Support Effect on Catalytic Activity of CO Oxidation. *Catal. Lett.* **2014**, *144*, 1411–1417.

(48) Zhang, N.; Yin, Y.; Xu, S.-J.; Chen, W.-S. 5-Fluorouracil: Mechanisms of Resistance and Reversal Strategies. *Molecules* **2008**, *13*, 1551–1569.

(49) Chambers, A. F.; Groom, A. C.; MacDonald, I. C. Dissemination and Growth of Cancer Cells in Metastatic Sites. *Nat. Rev. Cancer* **2002**, *2*, 563–572.

(50) Cory, S.; Adams, J. M. The Bcl2 Family: Regulators of the Cellular Life-or-Death Switch. *Nat. Rev. Cancer* **2002**, *2*, 647–656.

(51) Herceg, Z.; Wang, Z. Q. Functions of Poly(ADP-Ribose) Polymerase (PARP) in DNA Repair, Genomic Integrity and Cell Death. *Mutat. Res.* **2001**, *477*, 97–110.

(52) Handali, S.; Moghimipour, E.; Rezaei, M.; Ramezani, Z.; Kouchak, M.; Amini, M.; Angali, K. A.; Saremy, S.; Dorkoosh, F. A. A Novel 5-Fluorouracil Targeted Delivery to Colon Cancer Using Folic Acid Conjugated Liposomes. *Biomed. Pharmacother.* **2018**, *108*, 1259–1273.

(53) Sachdev, A.; Matai, I.; Gopinath, P. Carbon Dots Incorporated Polymeric Hydrogels as Multifunctional Platform for Imaging and Induction of Apoptosis in Lung Cancer Cells. *Colloids Surf., B* **2016**, *141*, 242–252.

(54) Carneiro, B. A.; El-Deiry, W. S. Targeting apoptosis in cancer therapy. *Nat Rev Clin Oncol* **2020**, *17*, 395–417.

(55) Qvarnström, O. F.; Simonsson, M.; Eriksson, V.; Turesson, I.; Carlsson, J. γ H2AX and Cleaved PARP-1 as Apoptotic Markers in Irradiated Breast Cancer BT474 Cellular Spheroids. *Int. J. Oncol.* **2009**, *35*, 41–47.

(56) Boulares, A. H.; Yakovlev, A. G.; Ivanova, V.; Stoica, B. A.; Wang, G.; Iyer, S.; Smulson, M. Role of Poly(ADP-Ribose) Polymerase (PARP) Cleavage in Apoptosis: CASPASE 3-RESISTANT PARP MUTANT INCREASES RATES OF APOPTOSIS IN TRANSFECTED CELLS. *J. Biol. Chem.* **1999**, *274*, 22932–22940.

Recommended by ACS

Biocompatible Red Blood Membrane-Carbon Dot Hybrids for Near-Infrared Imaging-Guided Chemotherapy

Shaobo Zhang, Hui Wang, *et al.*

MAY 11, 2023
ACS APPLIED NANO MATERIALS

READ 

Review of Carbon Dot-Based Drug Conjugates for Cancer Therapy

Naveet Dubey, Apurba Lal Koner, *et al.*

MARCH 13, 2023
ACS APPLIED NANO MATERIALS

READ 

Mitochondrial-Targeted Gold-Doped Porous Carbon Nanodots for Combined Photothermal and Photodynamic Therapy of Breast Cancer

Lirong Zhang, Fengyi Du, *et al.*

APRIL 18, 2023
ACS APPLIED NANO MATERIALS

READ 

Resveratrol Carbon Dots Disrupt Mitochondrial Function in Cancer Cells

Shani Ben-Zichri, Raz Jelinek, *et al.*

SEPTEMBER 06, 2022
BIOCONJUGATE CHEMISTRY

READ 

Get More Suggestions >